MASTER

IS-T- 862

Magnetic and electronic properties of Nd-La and Ce-La alloys

Thomas Sonke Petersen

Ph. D Thesis submitted to Iowa State University

Ames Laboratory, DOE
Iowa State University
Ames, Iowa 50011

Date Transmitted: May 1979

PREPARED FOR THE U.S. DEPARTMENT OF ENERGY
UNDER CONTRACT NO. W-7405-eng-82

NOTICE
This report was prepared as an account of work sponsored by the United States Government. Neither the United States nor the United States Department of Energy, nor any of their employees, nor any of their contractors, subcontractors, or their employees, makes any warranty, express or implied, or assumes any legal liability or responsibility for the accuracy, completeness or usefulness of any information, apparatus, product or process disclosed, or represents that its use would not infringe privately owned rights.

DISTRIBUTION OF THIS DOCUMENT IS UNLIMITED

DISCLAIMER

This report was prepared as an account of work sponsored by an agency of the United States Government. Neither the United States Government nor any agency Thereof, nor any of their employees, makes any warranty, express or implied, or assumes any legal liability or responsibility for the accuracy, completeness, or usefulness of any information, apparatus, product, or process disclosed, or represents that its use would not infringe privately owned rights. Reference herein to any specific commercial product, process, or service by trade name, trademark, manufacturer, or otherwise does not necessarily constitute or imply its endorsement, recommendation, or favoring by the United States Government or any agency thereof. The views and opinions of authors expressed herein do not necessarily state or reflect those of the United States Government or any agency thereof.

DISCLAIMER

Portions of this document may be illegible in electronic image products. Images are produced from the best available original document.

NOTICE

This report was prepared as an account of work sponsored by the United States Government. Neither the United States nor the United States Department of Energy, nor any of their employees, nor any of their contractors, subcontractors, or their employees, makes any warranty, express or implied, or assumes any legal liability or responsibility for the accuracy, completeness, or usefulness of any information, apparatus, product or process disclosed, or represents that its use would not infringe privately owned rights.

Available from: National Technical Information Service
U. S. Department of Commerce
P.O. Box 1553
Springfield, VA 22161

Price: Microfiche $3.00

TABLE OF CONTENTS

		Page
I.	INTRODUCTION	1
II.	THEORY	5
	A. Magnetic Ordering in Rare Earth Metals and Alloys	5
	B. Theory of Transport Properties	12
	1. Electrical resistivity	12
	2. Thermoelectric power	19
III.	EXPERIMENTAL PROCEDURE	29
	A. Sample Preparation	29
	B. Measurement of Electrical Resistivity	31
	C. Measurement of Thermoelectric Power	35
	D. Measurement of Magnetic Susceptibility	42
IV.	RESULTS	44
	A. Neodymium and Nd-La Alloys	44
	B. Ce-La Alloys	57
V.	DISCUSSION	69
	A. Magnetic Ordering Phenomena	69
	B. Kondo Effect in Ce-La Alloys	75
VI.	SUMMARY	81
VII.	BIBLIOGRAPHY	82
VIII.	ACKNOWLEDGEMENTS	87
IX.	APPENDIX	88
	A. Thermoelectric Power of Ce in a Crystal Field	88
	B. Tabulation of Experimental Data	91

Magnetic and electronic properties of Nd-La and Ce-La alloys

by

Thomas Sonke Petersen

A Dissertation Submitted to the
Graduate Faculty in Partial Fulfillment of
The Requirements for the Degree of
DOCTOR OF PHILOSOPHY

Department: Physics
Major: Solid State Physics

Approved:

In Charge of Major Work

For the Major Department

For the Graduate College

Iowa State University
Ames, Iowa

1979

I. INTRODUCTION

The rare earth metals are among the most exotic of elements in terms of their crystalline and magnetic structures. The localization of the 4f electrons allows a great variety of ferromagnetic, ferrimagnetic and antiferromagnetic structures. The number of 4f electrons increases monotonically across the series from La (0) to Lu (14) and there are some resultant trends in the magnetic properties. In general, the heavy rare earths, Gd, Tb, Dy, Ho, Er, and Tm, have large magnetic moments, dominant exchange energies, fairly high magnetic ordering temperatures, ferro- or ferrimagnetic structures, and simple hexagonal close-packed (hcp) crystal structures. The light rare earths, Ce, Pr, Nd, Pm, and Sm, have smaller magnetic moments, exchange energies comparable with crystalline electric field energies, low magnetic ordering temperatures, generally only antiferromagnetic structures, and complicated hcp crystal structures. The light rare earths are particularly difficult to work with because of the presence of several allotropes in a single sample, low melting temperatures, sample impurities, and their highly oxidant nature.

Recent metallurgical developments have made feasible more experiments on the light rare earth metals. First of all, single crystals of face centered cubic (fcc) γ-Ce and double hexagonal close-packed (dhcp) La, Pr and Nd can now be grown by using the levitation zone melting method of McMasters, Holland, and Gschneidner (1). Large single crystals of these materials are being studied by neutron diffraction, optical measurements, and magnetic and transport measurements.

Also, sample purification has been improved by the solid state electrotransport (S.S.E.) process (2). In addition, temperature cycling and annealing techniques (3) have made it possible to obtain single phase samples of dhcp Ce and dhcp Ce-La alloys. It is now possible to get rare earth samples of four 9's chemical purity and 99% allotropic purity.

Many measurements have been made on cerium since the discovery by Trombe and Foex (4) of the low temperature allotropes α-Ce (quadrivalent fcc), β-Ce (dhcp), and γ-Ce (trivalent fcc). Measurements of heat capacity (5) and electrical resistivity and magnetic susceptibility (6) have been made on pure β-Ce. These confirm that there are anomalies at 12.45K and at 13.7K which are presumably due to antiferromagnetic ordering. Neutron diffraction (7) on polycrystalline β-Ce found a complex antiferromagnetism below 12.5K. Single crystals of β-Ce have never been made and the exact magnetic structure is still unknown. La-Ce alloys also show a double peak in the heat capacity (8) but only one anomaly was seen in the resistivity (9) and magnetic susceptibility. However, the samples used in these measurements contained a considerable amount of fcc.

Cerium is normally trivalent with a single 4f electron which is quite close to the Fermi surface. This proximity of the 4f electron to the conduction electrons leads to effects such as the Kondo effect in dilute Ce alloys and a mixed valence phase (trivalent to quadrivalent) in Ce and Ce-La alloys under pressure. There are Kondo-like effects in the resistivity of nondilute Ce-La alloys (10) and

even in pure β-Ce (11). The electronic transport properties are also influenced by resonant scattering of the conduction electrons from the crystal field levels of the 4f electrons (12).

Measurements of the electrical resistivity and thermoelectric power are very sensitive to changes in the Fermi surface that arise from magnetic ordering. These measurements were undertaken on the Ce-La system to study the antiferromagnetic ordering and to resolve the double-peak anomaly in the heat capacity. In addition, these same measurements are interesting because the Kondo effect and the resonant scattering provide information about the exchange interaction.

Neodymium is also a trivalent light rare earth with three 4f electrons and has the dhcp crystal structure. Nd orders antiferromagnetically at 19.9K with moments modulated in the basal plane with a wave vector, $\vec{q}$, which varies from 0.144 (7 atomic spacings) at 19.9K to 0.125 (8 lattice spacings) at 8K (13). The exact magnetic structure of Nd is still uncertain but it has been determined that the neutron diffraction satellites are magnetic in nature (14) and not nuclear satellites caused by magnetic distortion of the lattice. Part of the difficulty in understanding the magnetic structure of Nd is the sample dependent effects. These may be resolved through measurements on better quality single crystals. Forgan et al. (15) have found a number of anomalies in the heat capacity of polycrystalline Nd between 5K and 8K which are believed to be due to magnetic effects. Previous neutron diffraction, magnetic susceptibility, and resistivity results have shown only one of these other anomalies at 7.5K and this was thought

to be a transition due to antiferromagnetic ordering on the cubic sites of the dhcp lattice (16). More likely it is a "lock-in" transition of the wave vector to the commensurate value of 0.125.

Lock (17) looked for magnetic ordering temperatures in the Nd-La alloy system. Only one ordering feature was found in his heat capacity and susceptibility measurements and this did not behave in a reasonable fashion as a function of concentration. One purpose of the present investigation was to search for additional magnetic features in the Nd-La alloys and to determine the correct magnetic phase diagram for this system. It is also an easier system to study than the Ce-La system because of the absence of the Kondo effect and the availability of single crystals of dhcp Nd.

This study is the first measurement of the thermoelectric power in nondilute Ce-La and Nd-La alloys and in single crystal Nd. Previous thermopower measurements include Ce-La at room temperature (18), dilute La-Ce (19) and polycrystalline Nd (20).

II. THEORY

A. Magnetic Ordering in Rare Earth Metals and Alloys

The unpaired 4f electrons are primarily responsible for the magnetic phenomena in the rare earths. The radial distributions of the 4f wavefunctions are closer to the nucleus than those of the filled $5s^2$ and $5p^6$ shells and the outer $5d^1 6s^2$ valence electrons. Because of the screening of the 4f electrons by the valence electrons as well as the small overlap of the 4f wavefunction with 4f electrons of neighboring atoms, these wavefunctions in the metal are much like the free atom wavefunctions with small perturbations. These electrons are said to be "localized" and the atom has a "localized (magnetic) moment". The size of this moment is determined by the free atom angular momentum quantum numbers ($\ell=3$; $m_\ell=3, 2, 1, 0, -1, -2, -3$; $s=1/2$; $m_s=\pm 1/2$) and Hund's coupling rules ($L=\Sigma m_\ell$; $S=\Sigma m_s$; $J=L-S$ for less than a half filled shell; $J=L+S$ for more than a half filled shell).

The magnetic properties of the rare earths may be understood by considering the effective Hamiltonian for the 4f electrons:

$$H = H_{ind\ ex} + H_{an\ ex} + H_{ms} + H_{cf} , \tag{1}$$

where the coulomb binding energy is left out. The first term is the indirect exchange interaction whereby the conduction electron spins are polarized by the presence of the 4f electrons and this polarization is felt by neighboring 4f electrons. This interaction between spins, $\vec{S}$, may be written:

$$H_{ind\ ex} = -\sum_{\vec{R}_{ij}} J(\vec{R}_{ij})\ \vec{S}_i \cdot \vec{S}_j , \tag{2}$$

where the exchange integral, J, is a function of the distance, $\vec{R}_{ij}$, between spins i and j. In general there is a strong spin-orbit coupling in the 4f shell so that $\vec{J}$ rather than $\vec{S}$ is a good quantum number. Using the projection of $\vec{S}$ on $\vec{J}$, $(g-1)\vec{J}$, the indirect exchange becomes

$$H_{ind\ ex} = -(g-1)^2 \sum_{\vec{R}_{ij}} J(\vec{R}_{ij})\, \vec{J}_i \cdot \vec{J}_j \ . \qquad (3)$$

The indirect exchange interaction can give rise to ferro- or antiferromagnetic coupling depending on the sign of J.

The second term of Equation 1 is the anisotropic exchange term which results from the asymmetry of the 4f wavefunctions. The third term is the magnetostrictive term. If the lattice is strained, there are forces on the spins caused by the change in the crystal field and also by the change in the anisotropic exchange.

The last term in Equation 1, the crystal field contribution, is very important in the light rare earth metals, although not as strong as in the 3-d transition metals where the crystal field breaks up the spin-orbit coupling and quenches the net orbital moment. The crystal field is due to electrostatic forces from the surrounding atoms in the lattice and therefore has the same symmetry as the lattice. The crystal field energy is small compared to the spin-orbit coupling in the rare earths so that it is treated as a perturbation which lifts the 2J+1 degeneracy of the 4f energy levels. The splittings of the resultant energy levels are typically on the order of 10-100K so that temperature dependent effects are seen in the low temperature heat capacity and magnetic susceptibility of these metals.

The crystal field potential energy may be written in the coulomb form:

$$H_{cf}(\vec{r}_i) = \int \frac{e\,\rho(\vec{R})}{(\vec{r}_i - \vec{R})}\, d\vec{R} \;, \tag{4}$$

where $\rho(\vec{R})$ is the charge density around the ion at $\vec{r}_i$. This energy is generally expanded in spherical harmonics $Y_\ell^m(\theta,\phi)$ where the polar coordinates (r, θ, ϕ) give the electron position. Then

$$H_{cf}(\vec{r}) = \sum_{\ell,m} A_\ell^m\, r^\ell\, Y_\ell^m(\theta,\phi) \;, \tag{5}$$

where the coefficients, A_ℓ^m, contain an integral over the charge distribution as in Equation 4. The spherical harmonics are then replaced with the Stevens (21) operator equivalent, O_ℓ^m,

$$H_{cf}(\vec{r}) = \sum_{\ell,|m|} V_\ell^m\, O_\ell^m \tag{6}$$

and $A_\ell^m \langle r^\ell \rangle$ is replaced with a new coefficient, V_ℓ^m. Because of the symmetry of the lattice most of the V_ℓ^m are zero and ℓ has a maximum value of 6.

La, Ce, Pr, and Nd are all stable in the double hexagonal close-packed (dhcp) structure at low temperatures. This has hexagonal layers of atoms stacked in the sequence (ABAC)(ABAC).... An atom in a given layer of the lattice will find its nearest neighbor atoms in either a cubic arrangement (A layers) or a hexagonal arrangement (B and C layers). Strictly speaking, the A layers have trigonal symmetry for which the crystal field energy, Equation 6, reduces to

$$H_{cf} = V_2^0\, O_2^0 + V_4^0\, O_4^0 + V_4^3\, O_4^3 + V_6^0\, O_6^0 + V_6^6\, O_6^6 \tag{7}$$

by group theory arguments. If the sites are indeed "cubic" then V_2^0

will also be zero. For the sites with hexagonal symmetry only the coefficients V_2^0, V_4^0, V_6^0, and V_6^6 are nonzero.

The Stevens operator equivalents, O_ℓ^m, are functions of the angular momentum, $\vec{J}$, of the 4f electrons and group theory arguments can give the degeneracies of the final wavefunctions as described in the book by Wallace (22). For cerium, where J = L-S = 3-1/2 = 5/2, a hexagonal crystal field splits the 2J+1 (6) levels into three doublets. A cubic crystal field splits the six levels into a doublet and a quartet. However, neodymium has J = L-S = 6-3/2 = 9/2 and the ten-fold degenerate states are split into five doublets by a hexagonal field and a doublet and two quartets by a cubic field.

The relative positions of these energy levels are determined from measurements of the heat capacity, low field magnetic susceptibility, inelestic neutron scattering, Mössbauer effect and indirectly from other measurements such as transport measurements. The Schottky anomaly in the specific heat is the easiest and most commonly used method but it is generally only applicable when there are no competing effects such as magnetic ordering in the vicinity of the Schottky peak. In the heat capacity of neodymium there are no broad peaks such as those normally attributed to crystal fields; there are only sharp peaks thought to be associated with the magnetic ordering. Lounasmaa and Sundström (23) tried to estimate the crystal field contribution to the heat capacity and fit this with possible crystal field configurations. This work indicated that quadrupole-quadrupole interactions may further split up the four-fold degenerate state into two doublets. Measurements

of inelastic neutron diffraction on neodymium (24, 25, 13, 14) have been partly successful in resolving the antiferromagnetic structure but have given little information about the crystal field levels. However a sharp jump in the size of the magnetic moments at 26 kOe has been attributed to level crossing of the crystal field levels.

Measurements of crystal field parameters in dhcp cerium are also inconclusive. In a cubic crystal field there is a ground state doublet and an excited quartet while a hexagonal field splits the six states into three doublets. Calculations by Bleaney (26) placed the quartet at 270K above the ground state and the doublets at 30 and 150K above the ground state. The 30K value has been shown to be too low by the heat capacity measurements of Lounasmaa and Sundström (23) and also by Panousis (27), who estimated that the doublets lie 85 and 110K above the ground state. Neutron diffraction measurements are best done on single crystals which are unavailable. However preliminary results on polycrystalline β-Ce indicated that the doublet excitations were at 98 and 113K and the quartet was at 206K (6).

The crystal structure plays a role in the exchange interaction, Equation 3. One may define the Fourier transformation of the exchange constant

$$J(\vec{q}) = \frac{1}{N} \sum_{i \neq j} J(\vec{R}_{ij}) \exp(i\, \vec{q} \cdot \vec{R}_{ij}) \ . \tag{8}$$

This quantity, $J(\vec{q})$, may be calculated from the band structure of the metal, but it contains matrix elements between conduction electron and f electron states which are difficult to evaluate in practice. These

are approximated as a simple function of $\vec{q}$, $I(\vec{q})$, so that

$$J(\vec{q}) = 2\ (g-1)^2\ (I(\vec{q}))^2\ \chi(\vec{q})\ , \tag{9}$$

where the generalized susceptibility, $\chi(\vec{q})$, is defined by

$$\chi(\vec{q}) = \frac{1}{N} \sum_{\vec{k}} (f_{\vec{k}+\vec{q}} - f_{\vec{k}})/(E_{\vec{k}+\vec{q}} - E_{\vec{k}}) \tag{10}$$

and $f_{\vec{k}}$ is the Fermi function of electrons with momentum $\vec{k}$ and energy $E_{\vec{k}}$. It may also be shown that if a magnetic structure is periodic with a wave vector $\vec{Q}$, then the exchange energy, Equation 3, becomes

$$H_{ind\ ex} = -A^2\ (g-1)^2\ J(\vec{Q})\ , \tag{11}$$

where A is a constant proportional to the magnetic moment, J. The wave vector, $\vec{Q}$, is determined by the maximum in $J(\vec{q})$ which is the same as the maximum in $\chi(\vec{q})$ if the exchange integral, $I(\vec{q})$, is fairly insensitive to $\vec{q}$. Because of the energy denominator, $E_{\vec{k}+\vec{q}} - E_{\vec{k}}$, in Equation 10, $\chi(\vec{q})$ is sensitive to flat areas of the Fermi surface which are separated by $\vec{q}$. In the hcp heavy rare earths there is a webbing feature in the Fermi surface which has large flat areas perpendicular to the c-axis. This so-called "nesting" of the q-vector results in a periodic magnetic order along the c-axis with a wave vector $\vec{Q}=\vec{q}$.

The Fermi surface of dhcp lanthanum (which should be similar to other dhcp light rare earths) has been computed by Fleming, Liu, and Loucks (28) and is shown in Figure 1. The electron and hole surfaces are shown as shaded areas on the surface of a wedge cut out of the hexagonal Brillouin zone. The most distinctive feature is the flat shelf which extends from the KM zone edge towards Γ. The authors comment that there are flat pieces of this shelf parallel to the ΓKHA

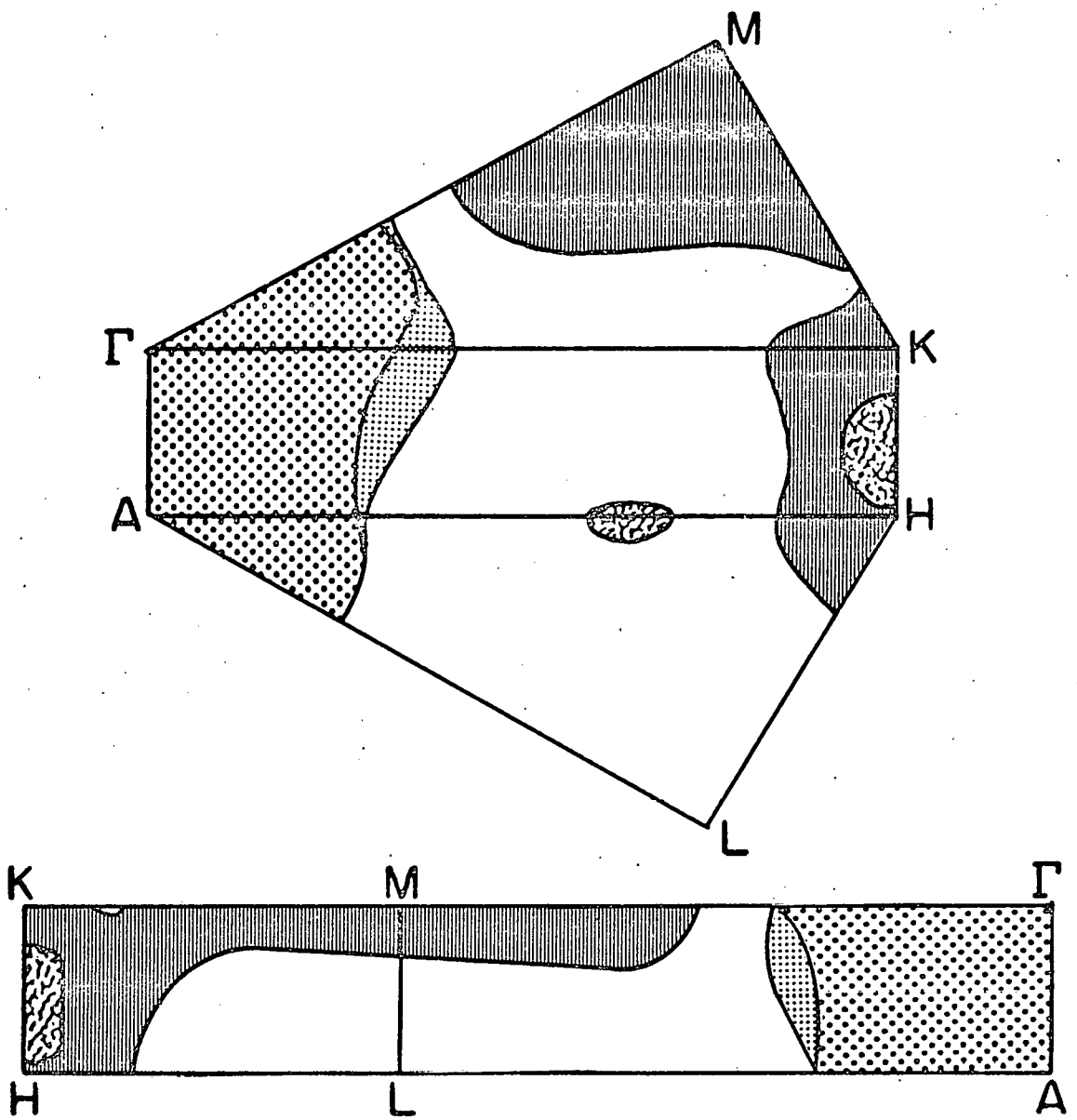

Figure 1. Fermi surface of dhcp La, Fleming, Liu and Loucks (28).

plane (along the b_1-axis) which are separated from each other by a wave vector of the same magnitude and direction as the observed wave vector of the magnetic order in Nd.

B. Theory of Transport Properties

1. Electrical resistivity

The electrical resistivity is a useful tool for studying magnetic materials because the magnetic moments may contribute to the scattering of conduction electrons in several ways. In general, anything which disrupts the periodicity of the lattice will tend to impede the flow of electrons. The scattering mechanisms which are important for the rare earths are:

(1) crystal defects (impurity ions, vacancies, etc.);

(2) lattice vibrations (phonon scattering);

(3) magnetic lattice vibrations (magnon scattering and spin disorder scattering);

(4) magnetic impurities (Kondo scattering).

The relative importance and the temperature dependence of these mechanisms will be discussed below.

Electrical resistivity is usually discussed using transport theory and the concept of relaxation time (29, 30). The resistivity tensor, ρ_{ij}, is expressed by the equation

$$(\rho_{ij})^{-1} = (e^2/4\pi^3\hbar) \int_{E_F} \tau \, v_i \, dS_j \, , \qquad (12)$$

where τ is the relaxation time, v_i is the i component of the electron velocity, and dS_j is the projection of a Fermi surface element in the

j direction. If the various scattering mechanisms are assumed to be independent, then Matthiessen's rule allows the scattering time, τ, to be written

$$\frac{1}{\tau} = \frac{1}{\tau_o} + \frac{1}{\tau_p} + \frac{1}{\tau_m} \tag{13}$$

where τ_o, τ_p, and τ_m are relaxation times due to the scattering processes of impurities, phonons, and magnons. Now if v_i may be replaced by its average value, v_{av}, then the total resistivity, ρ, becomes the sum of all of the resistivities of the individual scattering mechanisms:

$$\rho = \rho_o + \rho_p + \rho_m \tag{14}$$

where ρ_o, ρ_p, and ρ_m are the resistivities due to impurities, phonons, and magnons, respectively.

The resistivity due to nonmagnetic interactions with impurities and defects is temperature independent assuming that the number of such defects does not significantly alter the lattice and its elastic constants. This residual resistivity, estimated by extrapolating the measured resistivity to T=0, is usually a good indicator of the purity of the sample. In binary alloys, the residual resistivity often follows the Nordheim rule (31, p. 297):

$$\rho_o = (\text{constant})\ (x)\ (1-x) \tag{15}$$

where x is the concentration of one of the constituent elements.

The temperature dependence of the phonon resistivity may be described by the Block-Grüneisen formula (29, p. 364):

$$\rho_p = \frac{A}{m} \left(\frac{T}{\theta_D}\right)^5 J_5 \left(\frac{\theta_D}{T}\right) , \tag{16}$$

where A is a constant containing integrals over the Fermi surface, m is the ionic mass, T is the temperature, θ_D is the Debye temperature of the solid, and $J_5(x)$ is a Debye integral defined in reference 29. At high temperatures ($T \gg \theta_D$), J_5 is proportional to $(\theta_D/T)^4$ so that ρ_p is linear in T. At low temperatures ($T \ll \theta_D$), J_5 is a constant and ρ_p is proportional to T^5. In fact, the low temperature resistivity of many of the rare earth metals goes like

$$\rho = \rho_o + \rho_1 T^n , \tag{17}$$

where the exponent, n=2-5, (32) indicates whether the phonons (n=5) or the magnetic moments (n=2) are the dominant contributors to the temperature dependent resistivity in this regime.

The electrical resistivity at the Néel temperature, T_N, is affected by the onset of magnetic superzones. The period of the magnetic order in antiferromagnets is greater than the atomic lattice spacing. This lowers the overall symmetry and band gaps open up in the Fermi surface where the magnetic superzone planes (with wave vectors $\vec{Q}$) intersect the Fermi surface. This distorts the Fermi surface and lowers the area projected in the direction perpendicular to the direction of the magnetic moments. This theory is quantified by Elliott and Wedgewood (33) and explains the qualitative features in the resistivity of Dy, Ho, and Er. There is a maximum in $\rho_{c\text{-axis}}$ and an increase of slope in $\rho_{a\text{-axis}}$ below the ordering temperature.

The anomalies (changes in slope) seen in the resistivity near the

magnetic ordering temperatures of the rare earths are also partly due to the effects of spin wave (magnon) scattering. Well above the magnetic ordering temperature the magnetic moments are random and a mean field approximation is used to obtain the following expression for the spin-disorder resistivity (34):

$$\rho_S = (3\pi Nm/2\hbar e^2 E_F)\ V_d^{\ 2}\ (g-1)^2\ J(J+1)\ , \qquad (18)$$

where N is the number of atoms, m is the electron mass, and V_d is an exchange integral which measures the overlap of the conduction electron wavefunction and the 4f wavefunction. This resistivity is independent of the temperature. Below the magnetic ordering temperature the spin wave population (and hence the spin-wave scattering) decreases as the temperature is decreased. Mackintosh (35) obtained the following expression for spin-wave scattering in a ferromagnet at low temperatures:

$$\rho_S = C\ T^2\ \exp\ (-\varepsilon/kt)\ , \qquad (19)$$

where C is a constant, ε is the spin wave excitation energy and k is the Boltzmann constant. If ε is small compared to T_C (Curie temperature), Equation 17 reduces to the usual T^2 temperature dependence of the magnetic scattering.

Suezaki and Mori (36) have shown that in antiferromagnets the temperature derivative of the electrical resistivity in the vicinity of the Néel temperature may be written in terms of the reduced temperature, $t = (T-T_N)/T_N$, as

$$\frac{d\rho_s}{dT} = -C_1\ t^{-(\alpha+\gamma-1)}\ , \qquad T>T_N \tag{20a}$$

$$\frac{d\rho_s}{dT} = -C_2\ t^{-(\alpha+\gamma-1)} - D\ t^{(\beta-1)}\ , \quad T<T_N \tag{20b}$$

where D is a constant related to the superzone energy gap and C_1 and C_2 are constants proportional to the spin scattering. The constants α and γ are the critical indices of the specific heat and the magnetic susceptibility, respectivity, and are related through the scaling relation, $\alpha+2\beta+\gamma=2$. For a Heisenberg antiferromagnet $\alpha=0$ and $\gamma=4/3$ so that

$$\frac{d\rho_s}{dT} = -C_1\ t^{-1/3}\ , \qquad T>T_N \tag{21a}$$

$$\frac{d\rho_s}{dT} = -C_2\ t^{-1/3} - D\ t^{-2/3}\ , \quad T<T_N\ . \tag{21b}$$

This temperature dependence has been verified in antiferromagnetic Cr (37), although the spin scattering term is difficult to observe because of the superzone gap effect below T_N. Recent theories (38, 39) have found that very close to T_N the temperature derivative of the resistivity due to short range spin correlations is proportional to the specific heat:

$$\frac{d\rho_s}{dT} \sim C_p\ . \tag{22}$$

Well above the Néel temperature the temperature dependence becomes

$$\frac{d\rho_s}{dT} \sim t^{-1/2} \tag{23}$$

and the spin resistivity becomes the spin disorder resistivity, Equation 18.

The Kondo effect arises from the "spin-flip" scattering process in which a conduction electron scatters off a localized f electron and each reverses its spin in the process. The effect depends on the Fermi distribution of the conduction electrons and is inversely related to the energy difference between the conduction electrons and the localized electronic level. Kondo's (40) calculation of the resistivity (using a perturbation calculation to third order in the exchange coupling constant) yields a term proportional to $-\ln(T/T_k)$ where T_k is the Kondo temperature. This contribution results in a minimum in the total resistivity in the vicinity of T_k. Matho and Beal-Monod (41) were able to show that the exchange interaction between the magnetic impurities modified the Kondo resistivity:

$$\rho_k = A + B \ln(T^2 + T_{V_{sf}}^2)^{1/2} , \tag{24}$$

where $T_{V_{sf}}$ is a characteristic temperature proportional to the exchange energy, V_{sf}, and A and B are constants. The temperature dependence of the resistivity of both dilute Ce alloys (42) and β-Ce metal (6) can be described well using this theory. Liu <u>et al</u>. (11) considered the short range clustering of the moments near the Néel temperature, T_N, to show that the Kondo resistivity is quenched out at low temperatures in an antiferromagnet. At high temperatures ($T \gg T_N$) their theory agrees with Equation 24 and at low temperatures ($T \ll T_N$) the Kondo resistivity is exponentially small, in good agreement with the results on β-Ce.

The antiferromagnetic exchange, V_{sf}, between the conduction electrons and the f electrons results in hybridization (or mixing) of the two kinds of electronic states. The stronger the coupling, the

larger the Kondo effect, but at the same time the hybridization grows, the f electrons are less "localized" and the Kondo theory works less well. Schrieffer and Wolff (43) included hybridization in an effective exchange interaction, which for small hybridization leads to a Kondo effect. The Schrieffer-Wolff transformation gives the expression for this effective exchange:

$$J_{eff} \sim |V_{sf}|^2 \; U/\{\varepsilon_f(\varepsilon_f+U)\} \; , \tag{25}$$

where U is the Coulomb repulsion between spin up and spin down electrons in the same localized electronic state, and ε_f is the energy between this state and the Fermi level. Coqblin and Schrieffer (44) used this Schrieffer-Wolff transformation to show that the effective exchange in Ce alloys is negative (as it must be to produce a Kondo effect) and then to calculate the spin-disorder resistivity and Kondo resistivity. Comparison of their theory with experiment yields reasonable values of the exchange constant. The 4f level in Ce metal and Ce-La alloys is ~0.1 eV below the Fermi level and this difference decreases as pressure is applied or the temperature is decreased.

In the light rare earths the crystal field splitting can be of the same order of magnitude as the exchange energy. In the Kondo sideband model (45, 46) the spin of the f electron does not flip but rather the z-component, M, of the total angular momentum, $\vec{J}$, changes by one unit (i.e., to a different crystal field level). The effect produces a peak in the resistivity of Ce compounds and alloys at a temperature roughly equal to the crystal field splitting. Cornut and Coqblin (12) have shown that this is actually a resonant Kondo scattering effect between

the conduction electrons and the crystal field levels of the local moment. They also discovered that there may be more than one Kondo temperature, T_k, i.e., $\rho \sim \ln(T/T_{k_L})$ for $T<\Delta$, $\rho \sim \ln(T/T_{k_H})$ for $T>\Delta$, where Δ is the crystal field splitting.

2. Thermoelectric power

The thermoelectric power, or Seebeck coefficient, of a solid results from the fact that the carriers (electrons, phonons, magnons, etc.) of the heat current, $\vec{U}$, interact directly with the carriers (electrons) of the electric current, $\vec{J}$. In the presence of an electric field, $\vec{E}$, and a temperature gradient, $\vec{\nabla}T$, these currents are given by the Onsager-like equations

$$\vec{J} = L_{11}\vec{E} + L_{12}\vec{\nabla}T \ , \tag{26a}$$

$$\vec{U} = L_{21}\vec{E} + L_{22}\vec{\nabla}T \ , \tag{26b}$$

where each of the coefficients is in general a 3x3 tensor. These equations are valid if the driving forces, $\vec{E}$ and $\vec{\nabla}T$, are not too large and the Boltzmann equation may be assumed to be linear in these forces (29, p. 270). From these two equations the transport properties of a solid may be derived.

In the absence of a temperature gradient ($\vec{\nabla}T=0$) the above equations lead to

$$\vec{J} = L_{11}\vec{E} \tag{27}$$

$$\vec{U} = (L_{21}L_{11}^{-1})\ \vec{J} \tag{28}$$

and the identification of L_{11} as the electrical conductivity tensor,

$\sigma=1/\rho$, and $L_{21}L_{11}^{-1}$ as the Peltier coefficient, Π. The Peltier effect is a reversible heat flow in a circuit composed of two dissimilar metals. If one of the junctions of the circuit is held at a fixed temperature, the temperature of the other junction will rise or fall depending on the direction of an electrical current.

If there is no electric current then Equations 26a and 26b become

$$\vec{E} = -(L_{12}L_{11}^{-1})\ \vec{\nabla}T \tag{29}$$

$$\vec{U} = (-L_{12}L_{11}^{-1}L_{21} + L_{22})\ \vec{\nabla}T\ , \tag{30}$$

where the quantity $(-L_{12}L_{11}^{-1}L_{21} + L_{22})$ is the thermal conductivity, K, and the coefficient in Equation 29, $-L_{12}L_{11}^{-1}$, is defined as the thermoelectric power or Seebeck coefficient, S.

To measure S directly there must be a temperature gradient across the sample and hence a temperature gradient in the measuring circuit. In practice a circuit composed of two dissimilar metals, X and A, as in Figure 2a, is used. The voltage across the open ends, ΔV_{AX}, is given by

$$\Delta V_{AX} = -\oint \vec{E} \cdot d\vec{r}\ . \tag{31}$$

Using Equation 29 this becomes

$$\begin{aligned}
\Delta V_{AX} &= -\oint S\ dT \\
&= \int_{T_0}^{T+\Delta T} S_A dT + \int_{T+\Delta T}^{T} S_X dT + \int_{T}^{T_0} S_A dT \\
&= \int_{T}^{T+\Delta T} (S_A - S_X)\ dT \\
&= \int_{T}^{T+\Delta T} S_{AX}\ dT\ ,
\end{aligned} \tag{32}$$

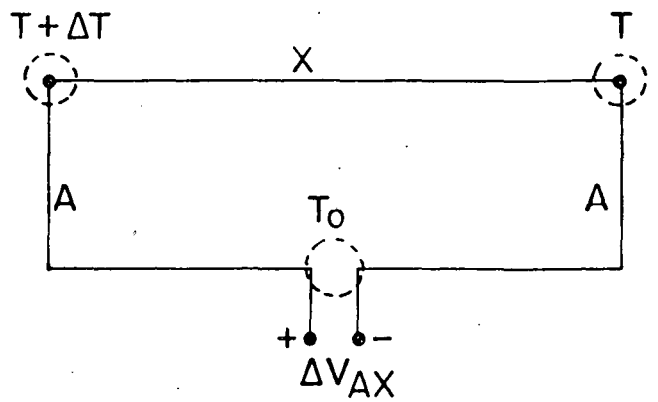

$$S_A - S_X = S_{AX} = \frac{dV_{AX}}{dT} = \lim_{\Delta T \to 0} \frac{\Delta V_{AX}}{\Delta T}$$

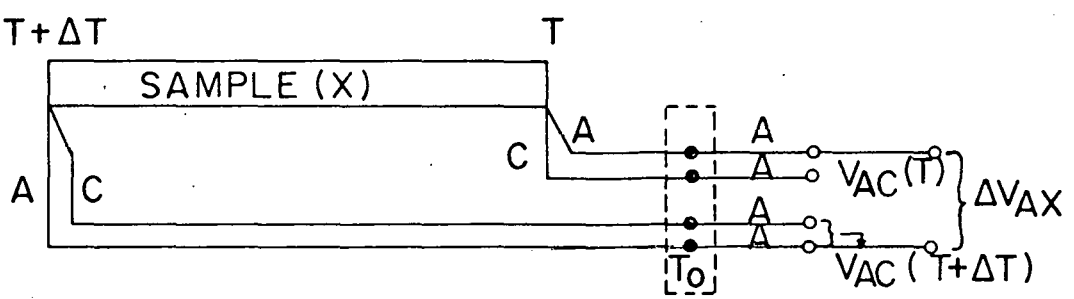

A = COPPER
C = CONSTANTAN OR AU-FE
$\Delta V_{AC} = V_{AC}(T+\Delta T) - V_{AC}(T)$
$S_{AX} = \Delta V_{AX}\ S_{AC}/\Delta V_{AC}$

Figure 2. Basic thermoelectric circuit
a) Sign convention
b) Wiring of thermocouples

where S_A and S_X are the absolute thermoelectric powers of each of the metals. The sign convention shown in Figure 2a is that when the voltage is measured from the hot junction to the cold junction, the thermoelectric power S_{AX} is the difference between that of the electrical leads and the unknown, S_A-S_X.

A final transport effect derived from Equations 26a and 26b is the Thomson coefficient, μ. If a metal has both an electrical current and a temperature gradient, then there is a change in the energy per unit volume, $\vec{Q}$, per unit time, t, given by

$$\frac{d\vec{Q}}{dt} = \vec{E} \cdot \vec{J} + \vec{\nabla} \cdot \vec{U} \ . \tag{33}$$

Substitution of Equation 26 and some algebra allows this to be written in terms of the transport coefficients σ, K, and S:

$$\frac{d\vec{Q}}{dt} = (\sigma^{-1} \cdot \vec{J}) \cdot \vec{J} + \vec{\nabla} (\vec{K} \cdot \vec{\nabla}T) - (T \frac{dS}{dt}) (\vec{J} \cdot \vec{\nabla}T) \ . \tag{34}$$

The first term of Equation 34 is the Joule heat produced by the electric current, the second term is the change in energy caused by heat flow, and the last term is a reversible heat which depends on the relative direction of $\vec{J}$ and $\vec{\nabla}T$. The coefficient of $\vec{J}\cdot\vec{\nabla}T$ is the Thomson coefficient:

$$\mu = T \frac{dS}{dT} \ . \tag{35}$$

The Thomson heat may be found by measuring the change in temperature caused by a reversal in $\vec{J}$. Knowing the Thomson heat allows one to calculate the absolute thermopower of a metal since from Equation 35

$$S(T) = \int_0^T \frac{\mu}{T} \, dT \ . \tag{36}$$

The thermoelectric power is generated by the flow of electrons and by the interaction of the flow of phonons and magnons with the electrons (phonon and magnon drag). In addition, these "sources" of thermopower are moderated by the various scattering mechanisms in the metal. To a first approximation the sources of the thermoelectric power may be assumed to be independent (47, p. 113) so that the total Seebeck coefficient, S, is the sum of the contributions from electron diffusion (S_D), phonon drag (S_p), and magnon drag (S_M). Each of these contributions is considered below.

The Seebeck effect is very sensitive to the size and shape of the Fermi surface. This may be seen by considering the expression for the diffusion thermopower derived using formal transport theory (48, p. 62):

$$S_D = (\pi^2 k^2 T/3e) \{\frac{\partial}{\partial E} \ln \sigma(E)\}_{E_F} , \tag{37}$$

where the electrical conductivity is given by

$$\sigma(E) = (e^2/12\pi^3\hbar) \int_E \tau \cdot v_i \, dS_j . \tag{38}$$

Now if the mean free path, $\Lambda(E) = \tau(E)\, v(E)$, varies slowly at the Fermi surface, then Equations 38 and 37 become

$$\sigma(E) = (e^2/12\pi^3\hbar)\, \Lambda(E)\, \Sigma(E) \tag{39}$$

$$S_D = (\pi^2 k^2 T/3e) \{\frac{\partial}{\partial E} \ln\Lambda(E) + \frac{\partial}{\partial E} \ln\Sigma(E)\}_{E_F} , \tag{40}$$

where

$$\Sigma(E) = \int_E dS . \tag{41}$$

The first term in Equation 40 is due to the various scattering mechanisms which will be discussed later. The second term depends on

the geometry of the Fermi surface. In general it gives a positive contribution to the thermopower for electron surfaces and a negative contribution for hole surfaces.

If the mean free path is independent of energy, then the diffusion thermopower of a simple free electron metal is easily obtained from Equation 40:

$$S_{D_0} = \pi^2 k^2 T/3eE_F \ . \tag{42}$$

This expression is a linear function of temperature and is most valid at high temperatures. The thermopower of most metals is experimentally found to be linear in T above the temperature at which phonon drag becomes negligible.

If the mean free path is not independent of energy, the contribution to the diffusion thermopower from each of the various scattering mechanisms must be considered. Consider a two component alloy with a solvent metal with resistivity ρ_j and an impurity metal which causes an impurity scattering contribution to the resistivity, ρ_j. Assuming the validity of Matthiessen's rule

$$\rho = \rho_i + \rho_j \tag{43}$$

and rewriting Equation 37 in terms of the total resistivity, $\rho = 1/\sigma$,

$$S_D = -(\pi^2 k^2 T/3e) \left\{\frac{\partial}{\partial E} \ln\rho(E)\right\}_{E_F} , \tag{44}$$

the diffusion thermopower then becomes

$$S_D = \frac{1}{(\rho_i + \rho_j)} \{\rho_i S_i + \rho_j S_j\} \tag{45}$$

where S_i is the thermoelectric power of the pure solvent metal and S_j is the intrinsic thermopower of the solute j in the host metal i,

$$S_j = -(\pi^2 k^2 T/3e) \{\frac{\partial}{\partial E} \ln\rho_j\}_{E_F} . \tag{46}$$

Equation 45 may be rewritten as the Gorter-Nordheim relation

$$S_D = S_i + \frac{\rho_j}{\rho} (S_j - S_i) . \tag{47}$$

A plot of S_D versus $1/\rho$ for a series of alloys at a fixed temperature should yield a straight line with an intercept of S_i and a slope of $\rho_j(S_j-S_i)$. In practice the total thermopower is used at temperatures at which the phonon drag contribution is negligible ($T<<\theta_D$ or $T>>\theta_D$). The Gorter-Nordheim rule is valid if the electronic band structure is independent of the impurity concentration. This usually requires that the solute and solvent have the same number of valence electrons. In addition, anisotropy of the electron scattering leads to a breakdown of Matthiessen's rule and makes the Gorter-Nordheim rule invalid.

When $\vec{\nabla}T \neq 0$, the phonons in the metal are not in thermodynamic equilibrium and may sweep electrons along via the electron-phonon interaction. At low temperatures ($T<\theta_D$) the phonon mean free path is long and the force on the electrons is proportional to the lattice heat capacity (density of phonons $\sim T^3$). At high temperatures ($T>\theta_D$) the phonon mean free path is short and the asymmetry of the phonon distribution due to $\vec{\nabla}T \neq 0$ is not communicated to the electrons. The mean free path due to phonon-phonon relaxation is proportional to 1/T. The temperature dependence of the phonon drag is given by Barnard (48, pp. 116, 138)

$$S_p \sim T^3 \ , \ T \ll \theta_D \tag{48a}$$

$$S_p \sim 1/T \ , \ T \gg \theta_D \ . \tag{48b}$$

The result is a phonon drag peak in the temperature range $0.1<T<0.2\theta_D$ which agrees well with experiment. If the electron-phonon interaction is dominated by Umklapp (U) processes, then S_p may change sign. At high temperatures few metals show the 1/T dependence of the phonon drag. This may be due in part to the competing effects of U and N-processes.

If $\vec{\nabla}T \neq 0$ in a magnetic material there will be a magnon current which gives rise to a magnon drag contribution to the thermopower. Bailyn (49) first studied this phenomenon and found that the temperature dependence is very similar to the phonon drag with a peak near 0.15 T_M, where T_M is the magnetic ordering temperature. However, the magnon specific heat is hundreds of times smaller than the phonon specific heat at temperatures near the magnon drag peak and hence the magnon drag peak is proportionately smaller than the phonon drag peak. This makes observation of the magnon drag effect difficult, but various investigators have reported seeing these effects in Fe at 200K, in antiferromagnetic Cr at 5<T<25K, and in Ni alloys at T<4.2K, and in heavy rare earths near 20K (50, p. 171; 32).

The same scattering mechanisms in the metal which are responsible for the electrical resistivity can modify the thermopower, particularly the electron diffusion component. Both phonon scattering and Kondo scattering may contribute thermopower peaks in addition to the phonon drag and magnon drag peaks.

The simple calculation of the electron diffusion thermopower, Equation 42, considers scattering by phonons or impurities only to first order and results in a linear temperature dependence. Nielsen and Taylor (51) calculated the corrections due to second order perturbation processes in which there is an intermediate phonon which is emitted and absorbed, or vice versa. These correction terms are strongly energy dependent near the Fermi level and can contribute greatly to the thermopower, Equation 37. At low temperatures the Nielsen-Taylor thermopower is proportional to $T^4 \ln T$ and approaches zero at high temperatures. The result is a peak in the range $0.1<T<0.2\theta_D$, which makes it difficult to separate from the phonon drag peak. The Nielsen-Taylor effect is sometimes called "phony phonon drag" since it is actually the electron diffusion thermopower.

In metals with magnetic impurities the Kondo scattering may yield a negative "giant thermoelectric peak" at low temperatures near T_k. Kondo (40) showed that the correct calculations of the thermopower must include both the spin-flip process and ordinary potential scattering. Then the diffusion thermopower associated with the Kondo effect is

$$S_K = -\left(\frac{k}{e}\right) \frac{2\pi^2 J^3 V n^2 S(S+1)}{(V^2 + J^2 S(S+1))} , \tag{49}$$

where J is the exchange scattering constant which must be negative, V is the nonmagnetic scattering potential of the impurity atoms, n is the density of states at the Fermi level, and S is the spin of the impurity moment. The denominator of this expression is proportional to the total resistivity. Therefore S_K decreases at high temperatures. Below the peak S_K decreases linearly as $T \to 0$. This is due to the Zeeman

splitting of the local moments. Even in the absence of long range magnetic order, there is a random local field, B, which becomes important when $kT<\mu_B B$.

The resonant Kondo scattering from crystal field levels near the Fermi surface produces effects in the thermopower as well as in the resistivity. Bhattacharjee and Coqblin (52) have shown that this mechanism will produce a peak or peaks in the thermoelectric power of alloys or compounds containing cerium. These peaks may be either positive or negative and occur in the range $(\Delta/6)<T<(\Delta/3)$ where Δ is the crystal field splitting. This theory explains the qualitative features of giant peaks in the thermopower of $Ce_{1-x}La_xAl_3$ compounds although the crystal field parameters obtained in the fit to the data do not agree with other measurements. The theory does not include interactions between magnetic ions so that it works best for dilute magnetic alloys.

The Seebeck effect is the most sensitive transport coefficient to changes in the Fermi surface because of the derivation in Equation 37. In the heavy rare earths there are abrupt anomalies in S(T) near the magnetic ordering temperatures. The decrease in the magnetic scattering below T_M will tend to increase the thermopower, but the Fermi surface will also tend to decrease because of the gaps at the magnetic superzone edges (53, p. 107). These competing effects make it difficult to predict the exact behavior of S near T_M. However, the Seebeck coefficient remains a useful tool for studying magnetic ordering phenomena.

III. EXPERIMENTAL PROCEDURE

A. Sample Preparation

The materials used in this work were prepared by K. A. Gschneidner's group in the Metallurgy and Ceramic Program of the Ames Laboratory, DOE. The Nd-La alloys were prepared by B. J. Beaudry, the Ce-La alloys by J. O. Moorman, and the Nd single crystals by O. D. McMasters. Both the $Ce_{1-x}La_x$ and the $Nd_{1-x}La_x$ alloy systems form solid solutions over the entire concentration range. All of the alloys were first prepared by melting together weighed amounts of the constituents. The Nd-La alloys were arcmelted over a copper hearth three times to insure sample homogeneity. They were then arccast into rod form and then annealed at 675 °C for one day, air cooled, and cut to size. The Ce-La alloys were first sealed in tantalum crucibles filled with inert gas. The crucibles were heated to the melting point of the constituents in an induction furnace and inverted and remelted three times. The samples were then removed from the crucibles by machining away the tantalum, cut to size, electropolished and resealed in tantalum crucibles. At this point two different heat treatments were used to get dhcp phase samples, depending upon the concentration of the Ce-La alloys. The La-rich alloys were annealed for several days at a temperature just below the dhcp to fcc phase transition which was typically 250 °C. The Ce-rich alloys were prepared by the method used to make β-Ce (3). In this procedure the samples are first heated to 400 °C and left overnight to produce single-phase fcc samples. These are cycled between room temperature and 4.2K ten times and then annealed

at 70 °C for seven days; this thermal cycling and annealing is repeated for a total of five times.

After the heat treatment, all of the samples were analyzed using an x-ray diffractometer and/or an x-ray camera. The Nd-La alloys were completely dhcp but the Ce-La alloys contained some fcc contamination. These results are discussed further in Chapter IV. The Ce-La alloys were cut to size using a diamond saw before the heat treatment. The Nd-La samples were cut from the heat treated ingots using a diamond saw and then polished to the final dimensions using sandpaper and electropolished. The resistivity and thermopower samples were approximately 1x1x20 mm and the magnetization samples were 3x3x5 mm with a mass of about 0.3 g.

The Nd single crystals were cut from larger ingots. These ingots were electropolished and examined visually and by x-rays for single crystals. The c-axis crystal was prepared by the solid state electrotransport process (2) in which high electrical currents are passed through a rod of Nd which is supported by a magnetic field to keep it from breaking. The Nd a-axis crystal was grown using the levitation zone melting method (1).

High purity starting materials were used in making all of the alloy samples. Typically there were about 20 ppma (parts per million atomic) of other rare earth metals, about 50 ppma of transition metals, and about 1000 ppma of nonmetallic impurities, primarily oxygen. The electrotransported Nd had only about 300 ppma of nonmetallic impurities. Care had to be taken, particularly with Ce-La alloys, to prevent

oxidation of the samples. The samples were stored under vacuum or an inert gas atmosphere and transferred to the cryostat as quickly as possible.

B. Measurement of Electrical Resistivity

The electrical resistivity was measured on most of the alloys from 1.2 to 300K and on all of the alloys from 1.2 to 30K. The measurements were made by the dc four-probe technique using a constant current through the sample and measuring the voltage between leads attached to the sample. The resistivity of the sample is given by

$$\rho = (V/I)\ (A/\ell) \tag{50}$$

where the voltage, V, divided by the electrical current, I, is the electrical resistance. A/ℓ is the ratio of the cross-sectional area to the distance between the voltage probes.

The current was supplied by a constant current supply which was designed and built by the Ames Laboratory electronics shop. This current supply gave currents from 10 to 150 mA and was stable to 1 part in 10^5. The sample current was held as low as possible, typically 10 to 25 mA, to prevent Ohmic heating of the samples. The voltage across the sample was measured with a Honeywell Rubicon Model 2768 potentiometer, a Guildline Model 9460A photocell amplifier, and a secondary galvanometer as the null detector.

The sensitivity of this voltage measurement is 5×10^{-9} volts so that for typical samples with a resistivity of 1-100 μΩ-cm the sensitivity of the measuring circuitry was about 10^{-3} μΩ-cm. The accuracy of the resistivity measurement was limited primarily by the

error in the sample geometrical factor, A/ℓ. The samples were made into as nearly perfect rectangular parallelopipeds as possible. The cross-sectional area was measured directly with a micrometer and averaged over several trials. The length between the voltage probes was measured with a traveling microscope. By making many measurements, the error in the resistivity due to the measurement of the A/ℓ factor was better than 0.5%.

The basic design of the dewar probe and sample holder is shown in Figure 3. The sample is held in place by the sharpened phosphor-bronze voltage probes. These probes are epoxied into a piece of copper or brass and hold the sample to the main copper block with a spring made from Ta wire. The sample is electrically insulated from the main block by a strip of mylar. Thermal contact is increased by the use of vacuum grease.

The temperature of the sample was cooled below 4.2K by pumping on ^{4}He which was condensed into the pump can. Temperatures above 4.2K were obtained by passing electrical current through a heater made from manganin wire (100Ω of No. 36 wire). The current was automatically controlled by a temperature controller constructed from a chopper stabilized operational amplifier which was described by Mellon (54). This controller looks at the out-of-balance signal from a Wheatstone bridge, one arm of which is a temperature sensor resistor and another arm a variable resistor to set the desired temperature. A 56 ohm carbon resistor was used as the sensor below 30K; above 30K a 150 ohm sensor of No. 38 Cu wire was used. Both the manganin heater and copper sensor

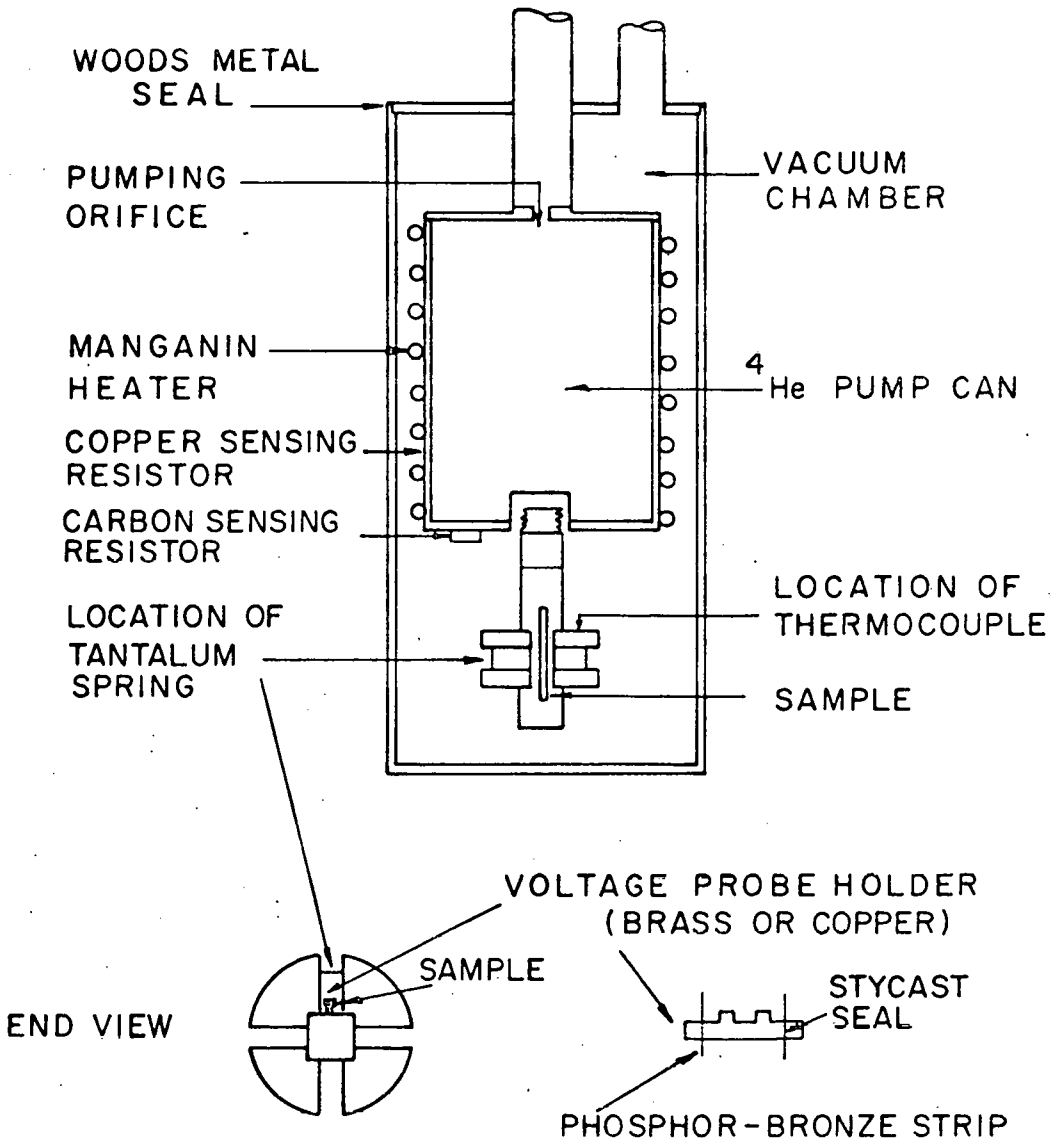

Figure 3. Resistivity probe and sample holder

were wound noninductively on the pump can with the copper sensor wound on first. A coat of GE No. 7031 varnish was applied over the top to insure good thermal contact. The leads to the sensors, heater, and sample current were made of No. 32 manganin wire and entered the vacuum space at the top of the probe through a nine pin vacuum tight connector.

The leads to the voltage probes were No. 38 copper wire and were continuous from the ice bath to the sample to reduce thermal emfs. To subtract out the remaining thermal emfs both the current through the sample and also the voltage leads at the potentiometer were reversed. The total emfs in the forward and reverse directions were averaged to obtain the actual emf across the sample.

The sample temperature was measured with a copper versus constantan thermocouple ($30K \leq T \leq 300K$) and gold-0.03% iron versus copper thermocouple ($T \leq 30K$). One junction of each thermocouple was anchored in the copper sample holder near the sample with Stycast epoxy and the other junction was in an ice bath. The master calibrations of Anderson et al. (55) for Au-Fe versus Cu thermocouples and Sparks et al. (56) for constantan versus Cu thermocouples were used. Each of the individual thermocouples was calibrated at four fixed temperatures (room temperature, the ice melting point, the N_2 boiling point, and the ^{4}He boiling point) and corrections made to the calibration tables following the procedure outlined by Eagen (57).

The thermocouple voltage was measured with a Leeds and Northrup K-5 potentiometer giving a temperature sensitivity of better than 0.01K. The accuracy of the constantan versus Cu thermocouple is estimated to be

±0.3K and that of the Au-Fe versus Cu thermocouple to be better than ±0.1K. The temperature controller maintained a stable temperature to better than ±0.01K for temperatures less than 10K and about ±0.05K for all other temperatures.

C. Measurement of Thermoelectric Power

Consider Figure 2a. If there is a small temperature gradient, ΔT, across the metal, X, then the voltage measured at the ends of the leads, ΔV_{AX}, is proportional to the difference between the thermopower of the leads, S_A, and that of the metal, S_X. For $\Delta T \ll T$ Equation 32 may be approximated

$$\Delta V_{AX} = (S_A - S_X)\ \Delta T = S_{AX}\ \Delta T\ . \tag{51}$$

To measure the thermopower of an unknown metal, the thermopower of the leads (Cu) must be determined. This can be done by measuring the relative thermopower of a known sample.

The thermoelectric probe and sample holder is shown in Figure 4. The dewar system and automatic temperature control system are the same as for the resistivity measurements. One end of the sample is soldered to a copper post which is anchored to the main copper block. The other end is soldered to a gradient heater assembly. The gradient heater is made from about 30 ohms of No. 34 manganin wire wrapped on a hollowed-out piece of Cu and is anchored with GE No. 7031 varnish. A Cu radiation shield is screwed over the sample and gradient heater. No exchange gas was used because of the problem of He adsorption on the surface.

The samples were soldered with indium to the Cu posts. It was

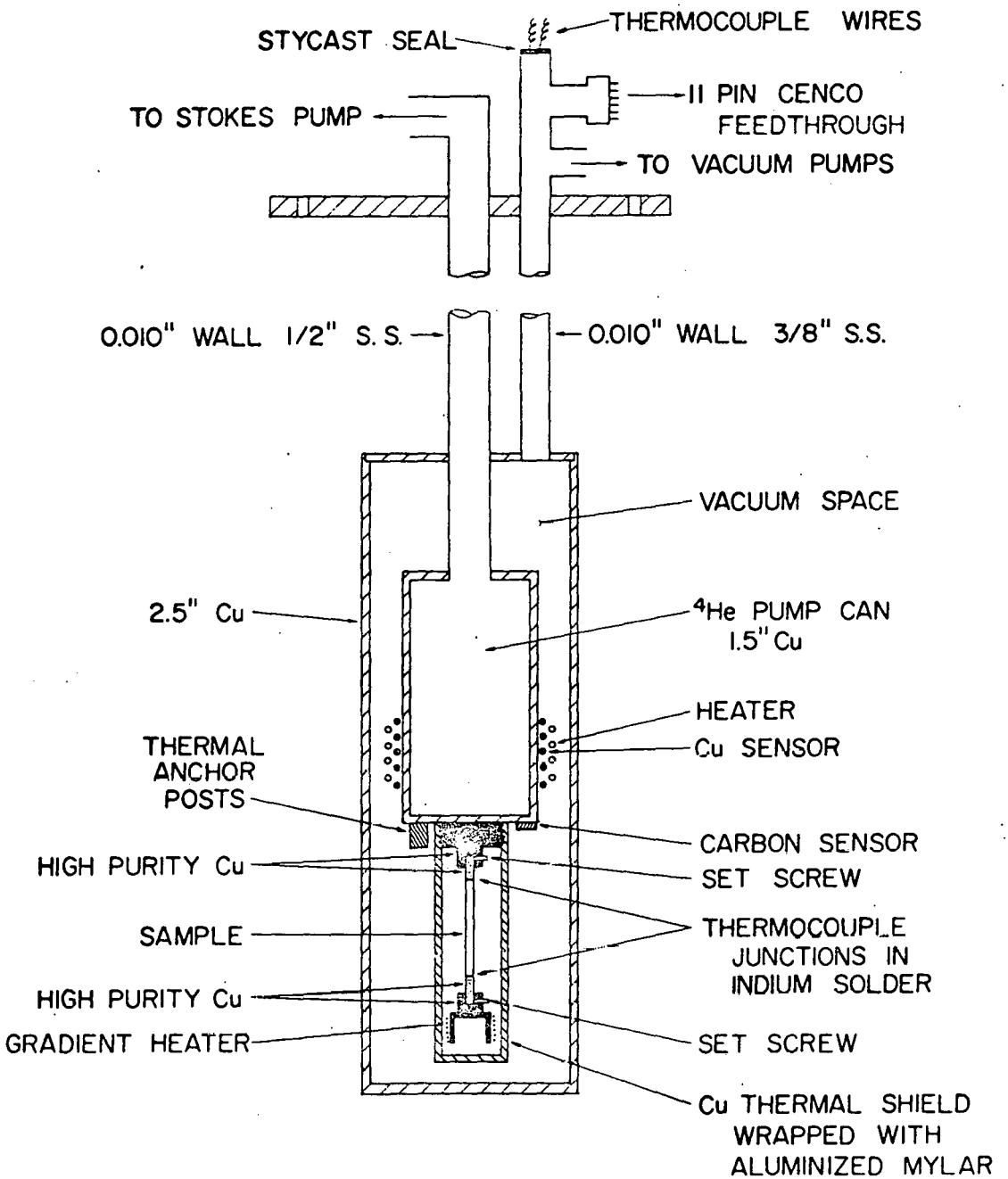

Figure 4. Thermoelectric probe and sample holder

impossible in open air to tin the ends of samples which contained La or Ce. A procedure that worked was to place the sample and an ultrasonic soldering iron inside an airtight plastic glove bag. The bag was pumped out and flushed with nitrogen gas several times. The surface of the metal was cleaned lightly with fine sandpaper and immediately tinned with indium.

Thermocouple junctions were soldered into the junction between the sample and the Cu posts. The basic thermoelectric circuit used is shown in Figure 2b. The emf between the two copper wires, A, is given by Equation 51,

$$\Delta V_{AX} = S_{AX}\ \Delta T + e_{AX}\ , \tag{52}$$

and the net emf difference between the hot and cold thermocouples, ΔV_{AC}, is given by

$$\Delta V_{AC} = S_{AC}\ \Delta T + e_{AC} \tag{53}$$

where S_{AC} is the sensitivity of the thermocouples and e_{AX} and e_{AC} are extraneous voltages caused by thermal gradients in the circuits. If e_{AX} and e_{AC} are small enough to be negligible or are subtracted from ΔV_{AX} and ΔV_{AC} then Equations 52 and 53 yield

$$S_{AX} = \Delta V_{AX}\ S_{AC}\ /\ \Delta V_{AC}\ . \tag{54}$$

Since ΔV_{AC} is the difference of two numbers which are generally relatively large but nearly equal, it is best to subtract $V_{AC}(T+\Delta T)$ and $V_{AC}(T)$ electrically. These thermocouples may not be placed directly in series without shorting out the sample. A Dauphinee comparator (53), Figure 5, which uses break-before-make gold-plated switches was used to

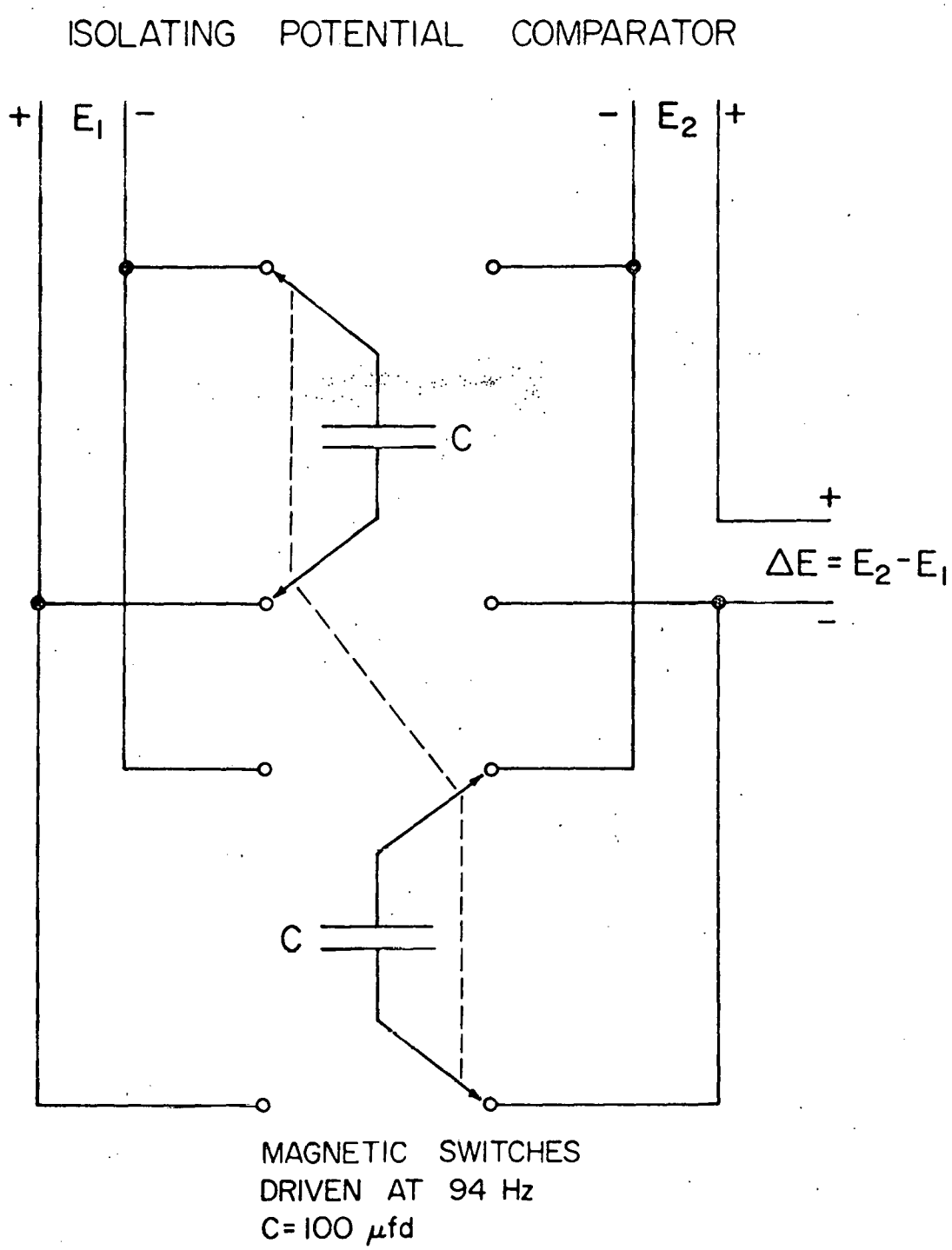

Figure 5. Dauphinee potential comparator

subtract these voltages. By putting the switches and capacitors inside an isothermal, shielded, grounded box and by keeping the switch contacts clean the noise could be kept below the detectable level of 0.005 μV.

The actual wiring of the thermoelectric power measuring circuit is shown in Figure 6. The Cu wires going from the sample to the ice bath were unbroken lengths of No. 38 Cu wire. All other unmarked wires were No. 20 Cu wire. The voltages ΔV_{AX} and ΔV_{AC} were measured with a Guildline 9180B potentiometer with a photocell amplifier and secondary galvanometer. The voltage sensitivity of this arrangement is better than 0.005 μV. The temperature gradients used varied from 0.5 to 3K depending on the spacing of data points. Hence in all cases the thermopower sensitivity was better than 0.01 μV/K. The accuracy of the data was about ±0.05 μV/K.

The thermal emfs, e_{AC} and e_{AX}, are minimized by avoiding rapid temperature changes along the wires. The thermocouple leads going from the sample up the stainless steel pumping line were inside teflon tubing which was placed inside a Pyrex tube to prevent the wires from touching the walls of the stainless steel. The remaining thermals were on the order of 0.1 μV. These were measured with $\Delta T=0$ and then subtracted from ΔV_{AC} and ΔV_{AX}.

The absolute Seebeck coefficient of the Cu leads, S_A, was determined by using a sample of 99.999% pure lead. The absolute Seebeck coefficient of lead, measured by Roberts (58), was then used to get S_A. Figure 7 shows S(T) as a solid black line. Also shown are previous

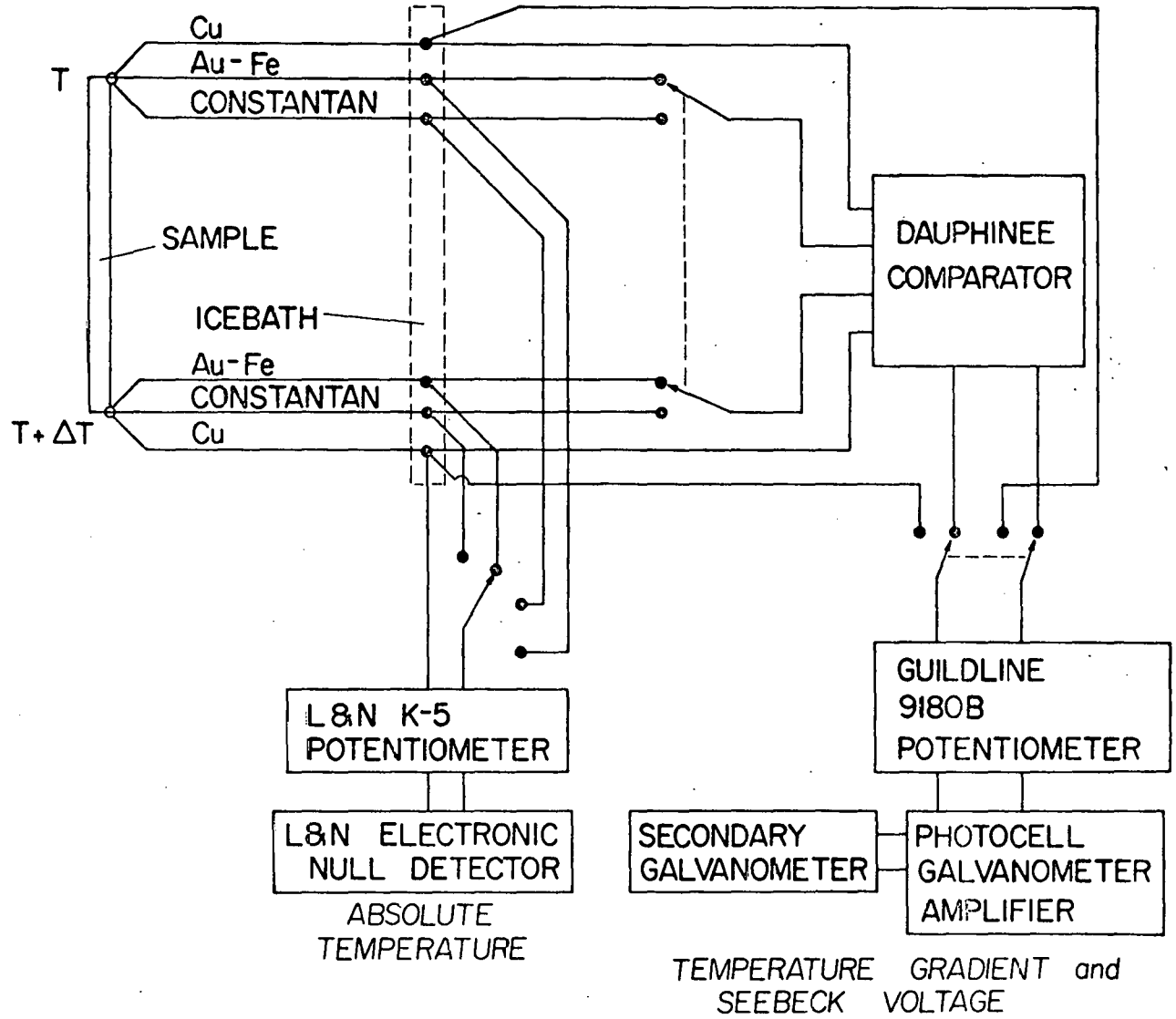

Figure 6. Complete circuit for measuring thermoelectric power

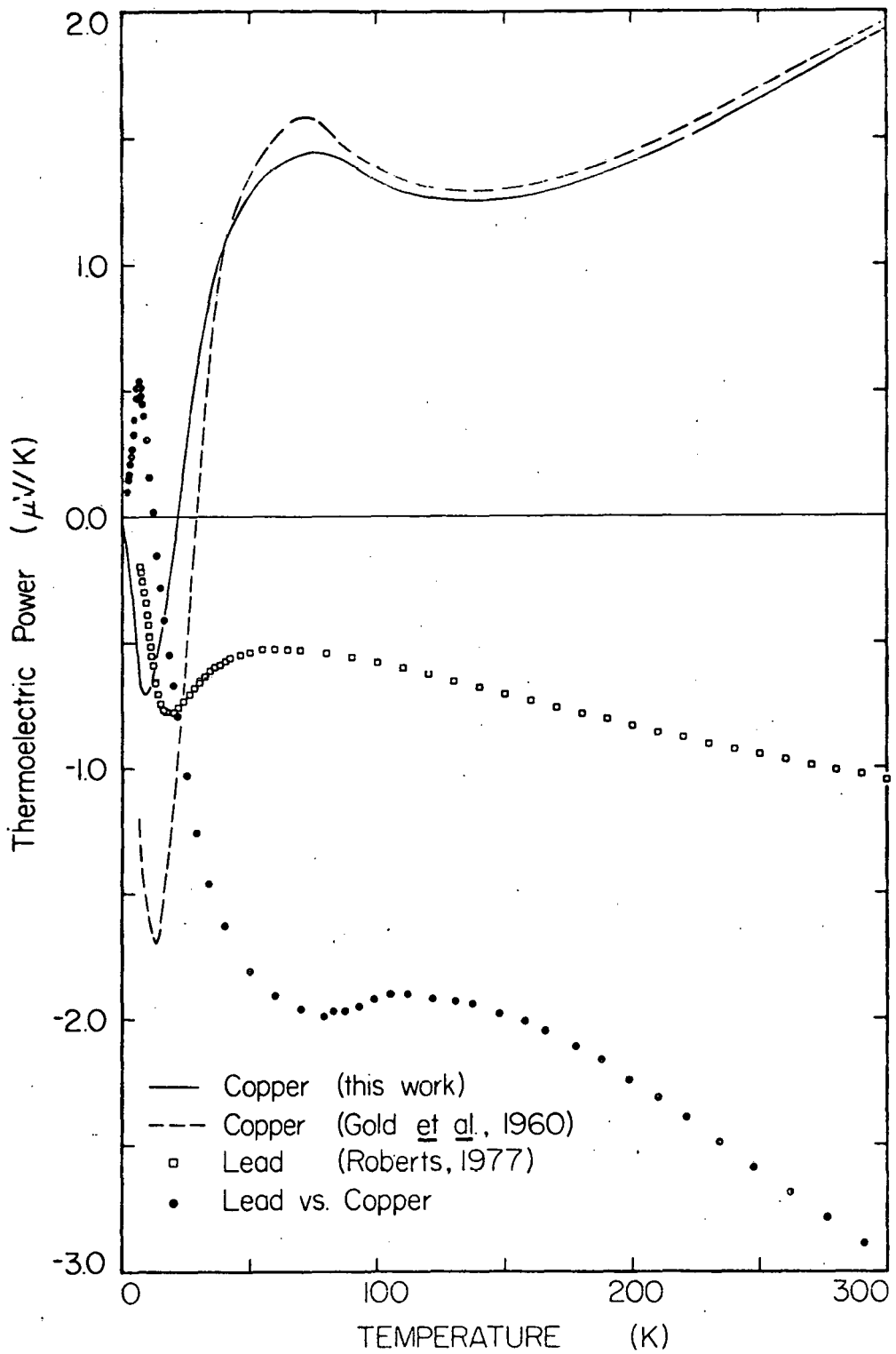

Figure 7. Absolute Seebeck coefficient of Cu leads

measurements on "pure" Cu (59) which agree with this work except at low temperatures. The low temperature negative peak (Kondo scattering) is very sensitive to the amount of Fe impurities and whether or not they are oxidized.

D. Measurement of Magnetic Susceptibility

The magnetic susceptibility of a magnetic material above its ordering temperature is given by the Curie-Weiss law

$$X = \frac{C}{T - \theta_p} \tag{55}$$

where C is the Curie constant

$$C = \frac{N\ J(J+1)\ g^2\ \mu\ B^2}{3k_B} \tag{56}$$

and θ_p is the product of C and the exchange interaction between moments. N is the number of atoms per unit volume. For antiferromagnets θ_p is negative. In practice $|\theta_p|$ is close but not equal to the magnetic ordering temperature because of deviations from Equation 55 near T_C or T_N. For an antiferromagnet χ is maximum at T_N and a plot of $\chi(T)$ shows a characteristic cusp at T_N.

A vibrating sample magnetometer, VSM, was used to measure the magnetization, M, of the samples as a function of temperature and applied magnetic field, H. The susceptibility may then by computed

$$\chi(T) = \lim_{H \to 0} M(T)/H\ . \tag{57}$$

The VSM vibrates the sample perpendicular to the applied magnetic field. Nearby coils of wire pick up an AC voltage which is proportional to the

magnetization of the sample. A lock-in amplifier measures this signal. This is not an absolute measurement so that the voltage must be calibrated with a Ni sample of known magnetization. All the samples have the same size, shape and orientation as the Ni standard so that it is not necessary to consider the depolarization factor. The samples were rectangular parallelopipeds measuring 3x3x5 mm and having a mass of about 0.3 g.

The VSM design has the advantage of allowing measurements of the magnetization over several orders of magnitude. The accuracy of this VSM is about 0.2% with a typical rare earth sample. The sensitivity is about 10^{-5} emu. This VSM was constructed by P. Burgardt and details of the design and operation may be found in his dissertation (60).

IV. RESULTS

A. Neodymium and Nd-La Alloys

The electrical resistivity of neodymium single crystals is shown in Figure 8. The c-axis sample was electrotransported and shows a lower residual resistivity than the a-axis sample. The resistivity ratios ($R_{300K}/R_{1.2K}$) are 27 for the c-axis sample and 16 for the a-axis sample.

The resistivity is nearly linear in temperature from 100-300K and shows anomalies at low temperatures. The low temperature data, shown on an enlarged scale at the bottom of Figure 8, exhibits three temperatures at which there is a change in the slope of $\rho(T)$. T_1 (19.0K) is the antiferromagnetic ordering temperature. The anomalies T_2 (8.0K) and T_3 (6.1K) are also present in both samples.

The anomalies are more visible in the plots of the second temperature derivative of the resistivity. A decrease in the slope of $\rho(T)$ as the temperature is increased results in a negative peak in $d^2\rho/dT^2$. The second derivative is computed numerically from the $\rho(T)$ data. At every temperature, T_i, n consecutive values of $\rho(T)$ in the vicinity of T_i are fit to a second order polynomial, $\rho = AT^2 + BT + C$, using a least squares approximation. Then $d^2\rho/dT^2|_{T_i}$ is equal to 2A. With a limited number of data points the choice of n is critical. If n is too small, small experimental errors in $\rho(T)$ will result in large scatter in $d^2\rho/dT^2$; if n is made too large, sharp structure in $d^2\rho/dT^2$ is averaged out. Typically the spacing of experimental data is 0.3K around the ordering temperature and the choice of n=5 gives plots of $d^2\rho/dT^2$ which show the anomalies with a resolution of better than 1.0K.

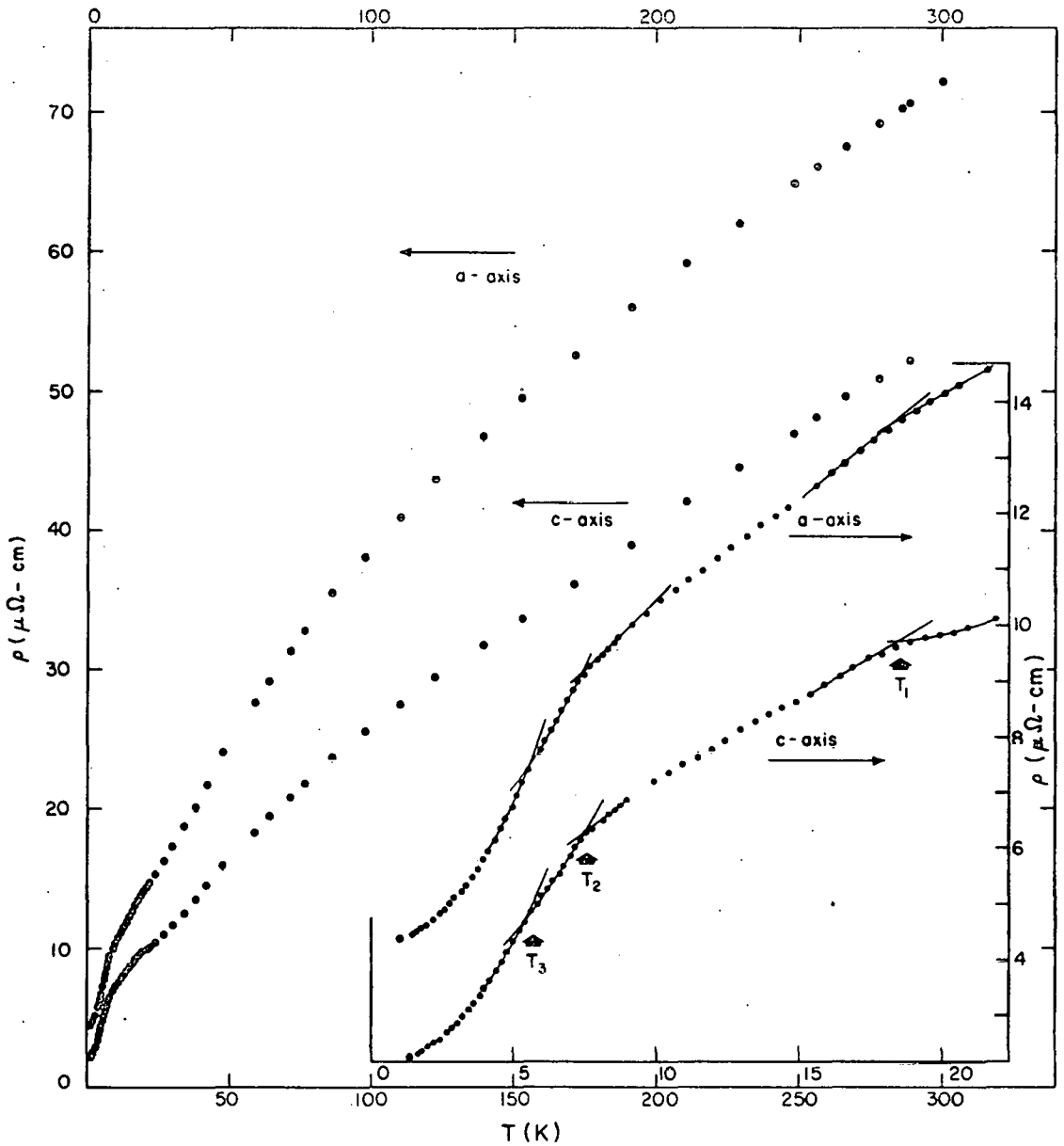

Figure 8. Electrical resistivity versus temperature of a-axis and c-axis neodymium

The second derivative of the resistivity of neodymium is shown in Figure 9. Negative peaks are seen at about the same temperatures, T_1, T_2 and T_3, as the anomalies in Figure 8. In the c-axis data the anomaly at T_2 appears to be a double peak, although the size of this effect is of the same order of magnitude as the scatter in the data. The anomaly at T_4 has not been reported in any other measurement on Nd. The effect is small, but the fact that it appears in both of the samples indicates that it may be a real effect. The interpretation of these anomalies in terms of magnetic ordering phenomena is discussed in the next chapter.

The thermoelectric power of neodymium is shown in Figure 10. The same crystals were used for the resistivity and thermopower measurements. Again there are anomalies at 19.0K and at 8.0K as indicated by the arrows. However these are relatively small in view of the large anomalies which occur in the thermoelectric power of other rare earth metals at the magnetic ordering temperatures (61). Figure 10 also shows a small negative peak in the vicinity of 50K which is probably the phonon drag peak. The shape of the thermopower from 100 to 300K is typical for rare earth metals. S(T) is nearly linear in temperature at room temperature as it should be if electron diffusion is the main contribution to the thermopower. The thermopower of the c-axis sample changes sign near 7K but this is not seen in the a-axis or in previous polycrystalline measurements.

The electrical resistivity of polycrystalline dhcp Nd-La alloys is shown in Figure 11. Also shown is data on dhcp La (62). Assuming the validity of Matthiessen's rule, Equation 14, the resistivity may be

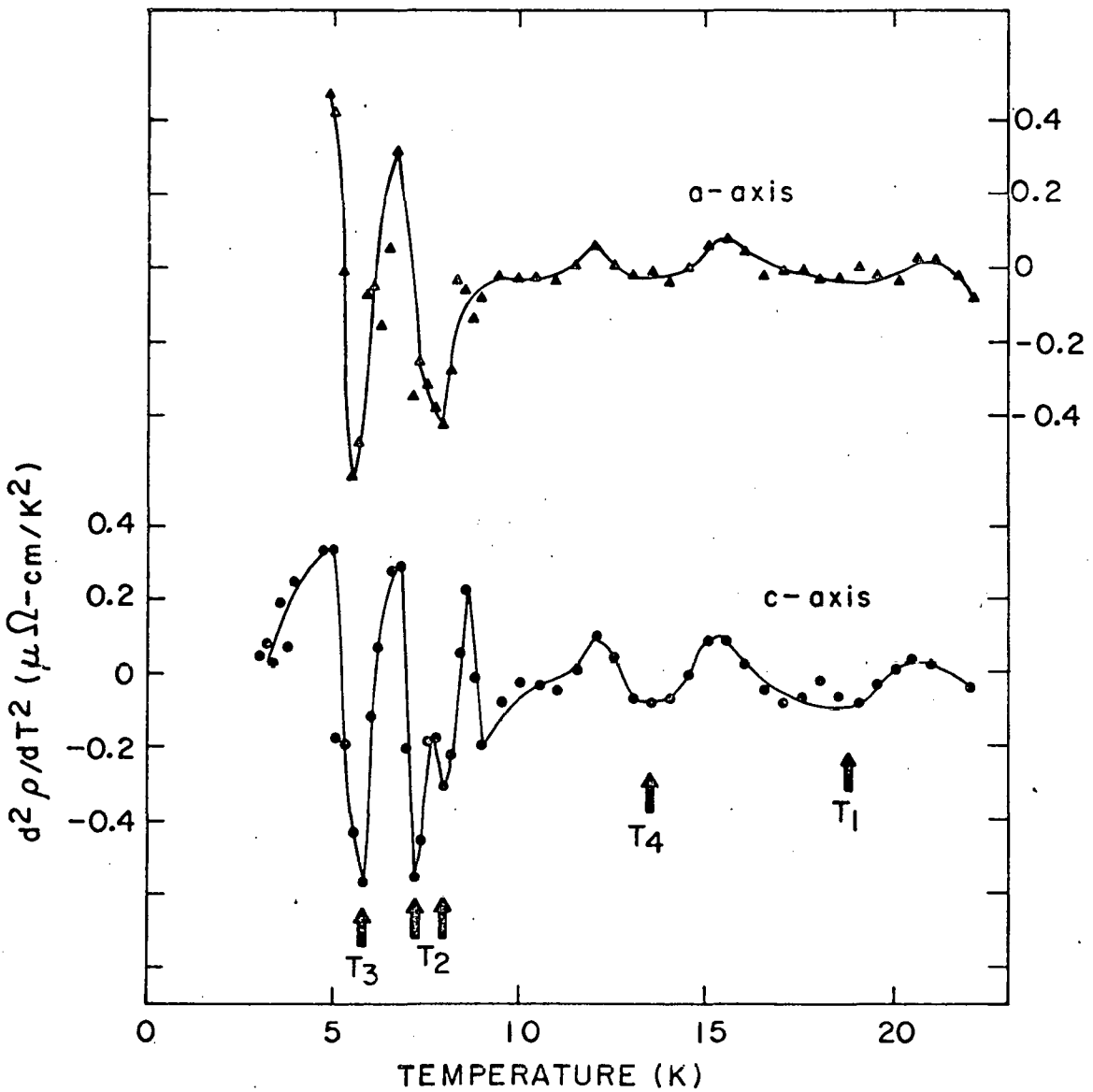

Figure 9. Second derivative of the resistivity of neodymium

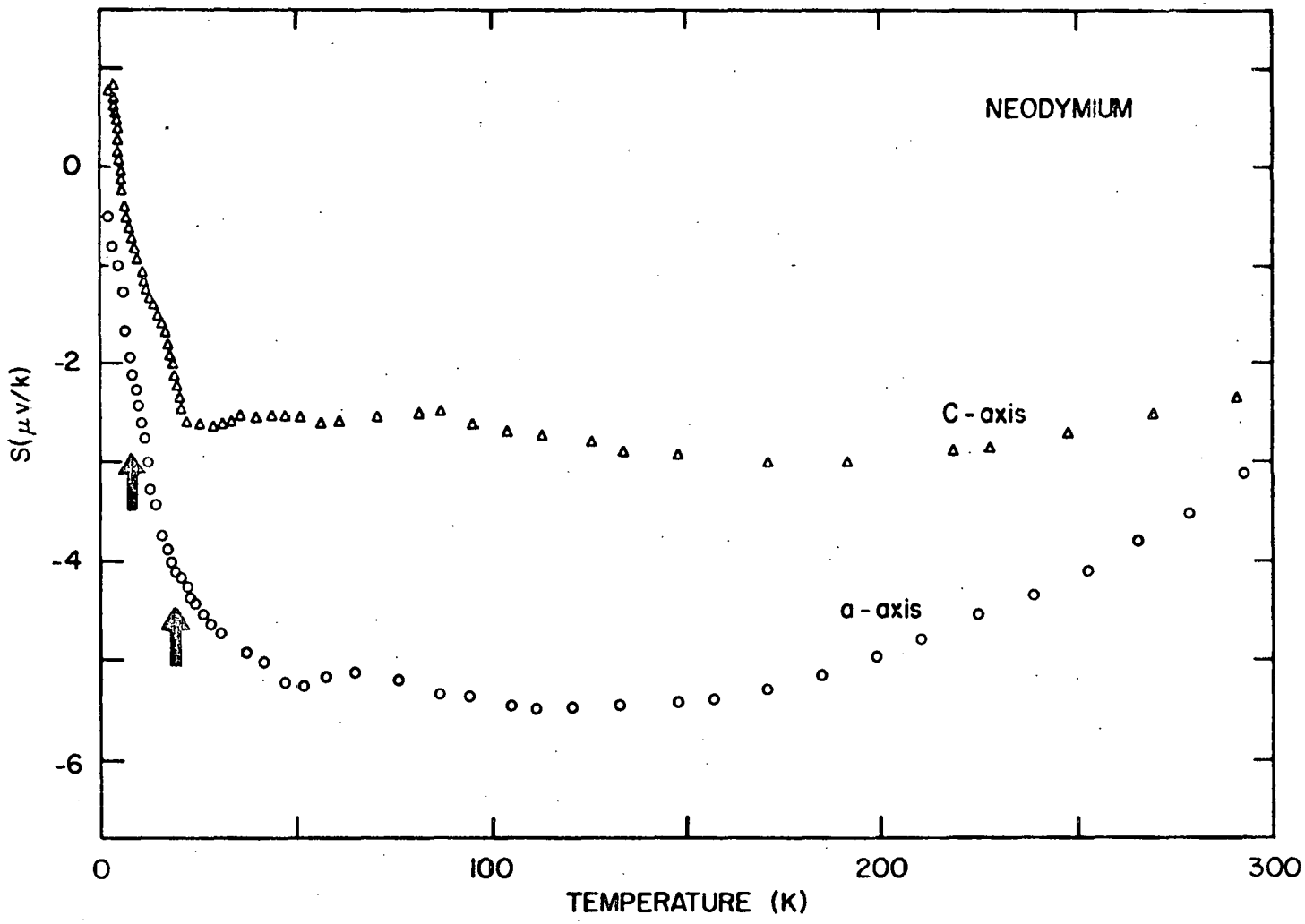

Figure 10. Thermoelectric power versus temperature of a-axis and c-axis neodymium

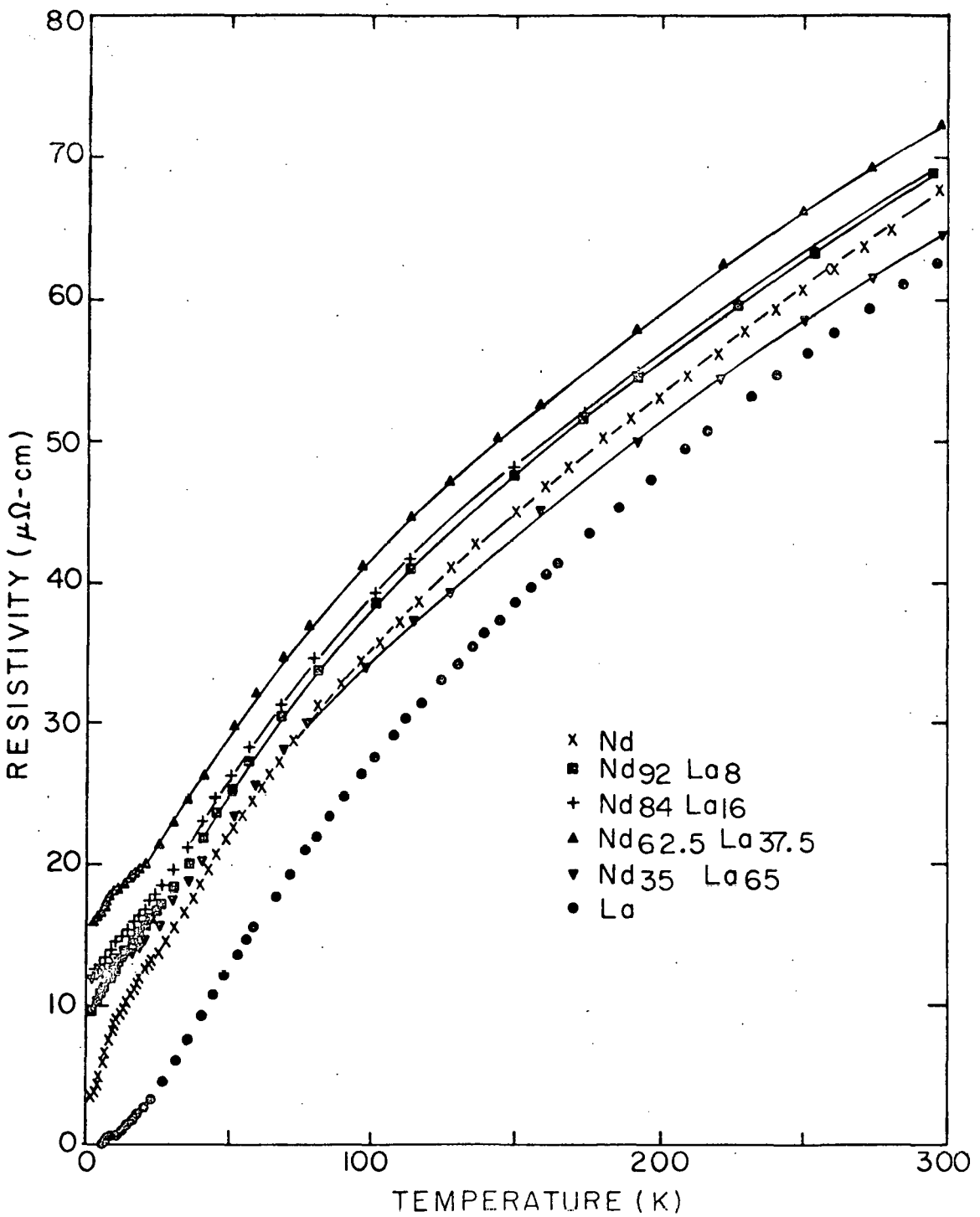

Figure 11. Electrical resistivity versus temperature of Nd-La alloys

written as the sum of the impurity (ρ_0), phonon (ρ_D) and magnon (ρ_M) contributions. The impurity contribution should be temperature independent and is greatest for the intermediate concentration alloys according to the Nordheim rule, Equation 15. This explains the high residual and total resistivities for the $Nd_{62.5}La_{37.5}$ sample. Above the magnetic ordering temperature the resistivity due to magnon scattering should be the temperature independent spin disorder resistivity, Equation 18. Hence the temperature dependence of the resistivity should be dominated by the phonon scattering which is linear. Figure 11 shows that all of the Nd-La alloy resistivities are nearly linear in temperature at 300K and the slopes are nearly equal. This is to be expected since the ionic masses (144 for Nd and 139 for La) and Debye temperatures (157K for Nd and 142K for La, 63) are very similar.

The resistivities of all of the polycrystalline Nd-La alloys show at least one and usually two magnetic ordering features of the same type as that found in the single crystal Nd data. The low temperature thermopowers of some of these same alloys, Figure 12, also have small features at the same temperatures which are generally small cusps or changes in the slope. The Nd c-axis sample shows the largest anomaly of any of these samples with a shallow maximum and minimum near 7.5K. This same sample has a positive peak at 3K which is probably not related to magnetic ordering, but probably due to either Umklapp processes beginning to dominate the phonon drag (because of the Fermi surface geometry) or to the Nielsen-Taylor effect. It is difficult to distinguish between these two effects based on these data because the

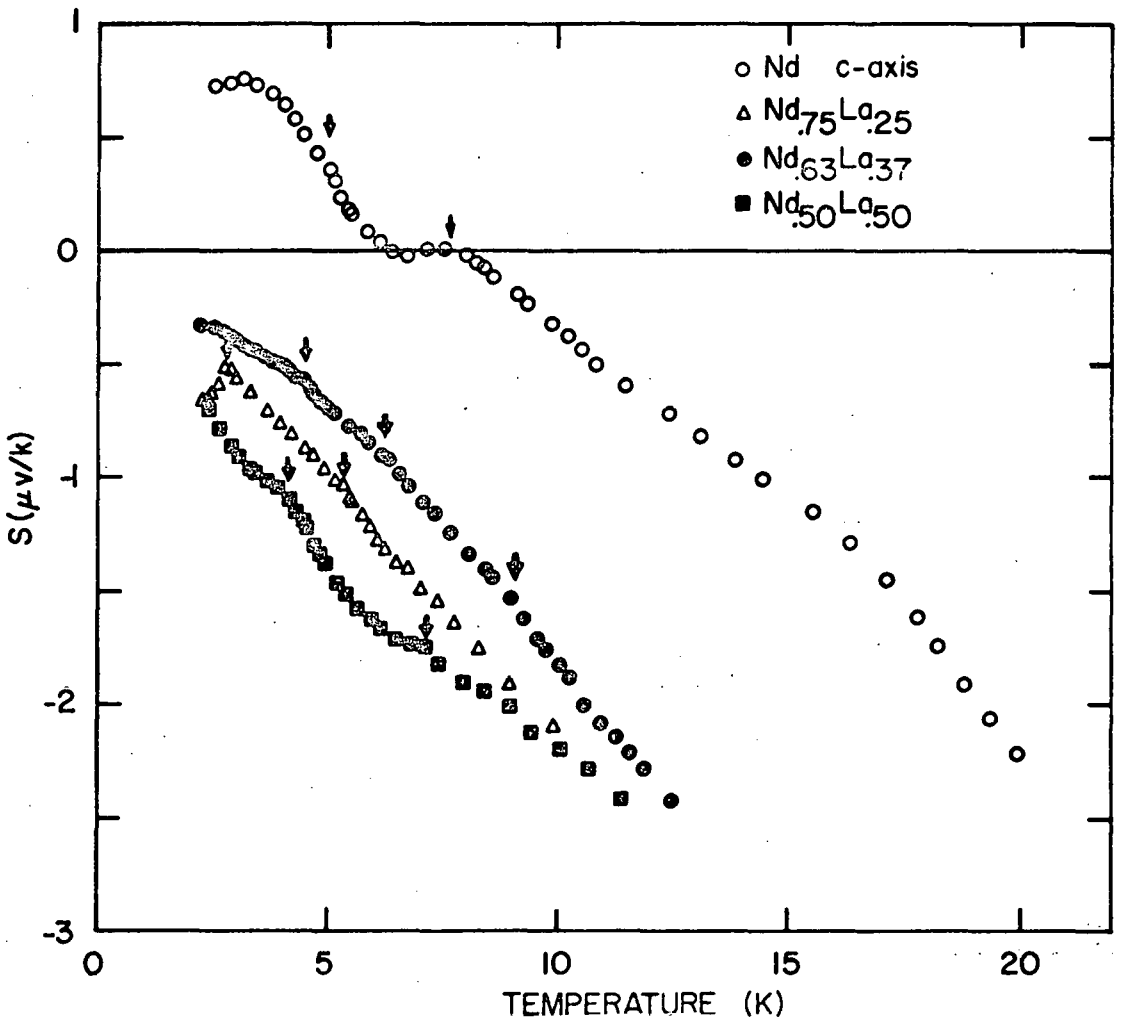

Figure 12. Low temperature thermopower of Nd and Nd-La alloys

temperature dependences of the peaks of the real phonon drag and the Nielsen-Taylor effect (phony phonon drag) are so similar. However the anisotropy of the effect makes the former explanation seem more plausible.

The higher temperature part of the thermopower of Nd and the $Nd_{50}La_{50}$ alloy, shown in Figure 13, does not change much qualitatively with the addition of La. An average of the single crystal data is computed using the formula

$$S_{poly} = (1/3)\ S_c + (2/3)\ S_a\ , \tag{58}$$

where S_a and S_c are the single crystal thermopowers. This equation is merely an approximation and a correct expression would include a factor inversely proportional to the resistivity of each of the single crystals. Since the temperature dependences of the resistivities are nearly identical, Equation 58 is valid and the results obtained by this method are in good agreement with the thermopower of polycrystalline Nd measured by Born, et al. (20). Figure 13 shows that the Nd-La alloys have a small peak near 50K which is due to phonon drag. The electron diffusion thermopower shows a small deviation from linearity at higher temperatures.

The magnetization, M, of the Nd-La alloys is measured at low temperatures at constant applied field, H. The magnetic susceptibility is taken to be $\chi = M/H$. At the Néel temperature (T_1 = 19K for Nd) the susceptibility shows a small change in slope but continues to increase as the temperature decreases until the second ordering temperature is reached. Here there is a peak in $\chi(T)$ which is broadened by the finite

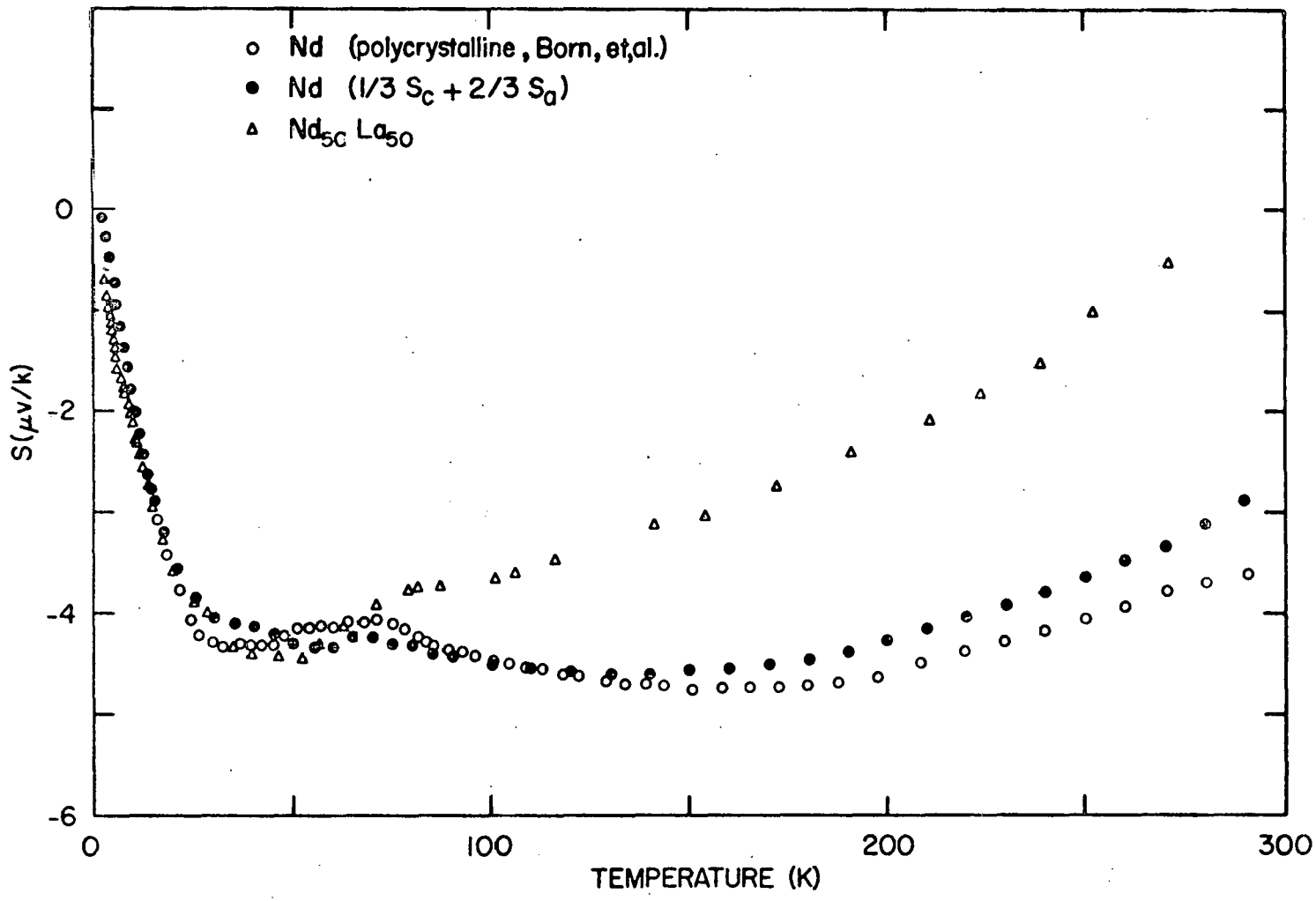

Figure 13. Thermoelectric power of polycrystalline Nd (Ref. 20) and $Nd_{50}La_{50}$

size of the applied magnetic field, typically 100 to 2000 Oe.

The susceptibility is Curie-Weiss like (χ proportional to 1/T) at temperatures above the ordering temperature. The effective magnetic moment, μ_{eff}, can be computed from the slope of $1/\chi(T)$ in the linear region. The paramagnetic ordering temperature, θ_p, is found by extrapolating $1/\chi$ to zero and taking the temperature intercept. Over a wide temperature range the inverse susceptibility is not exactly linear and Lock (64) showed that the susceptibility of Nd may be written in the Curie-Weiss form plus a temperature independent term

$$\chi = \frac{9.47 \times 10^{-3}}{T - 4.3K} + 5.0 \times 10^{-6} \text{ emu/g} . \qquad (59)$$

The values of μ_{eff} and θ_p were computed from the slope of $1/\chi(T)$ at low temperatures where the constant term of Equation 59 is negligible. These are shown in Table 1, along with published data on Nd (64, 65).

Table 1. Magnetic parameters of Nd and Nd-La alloys

Alloy	θ_p(K)	μ_{eff}(μ_B/atom Nd)	T_N(K)	Reference
Nd	4.3	3.3		64
Nd c-axis	0	3.45	19	65
Nd a-axis	5	3.45	19	65
$Nd_{84}La_{16}$	9.1	3.7	14.1	
$Nd_{75}La_{25}$	10.5	3.9	12.8	
$Nd_{63}La_{37}$	10.3	4.0	10.0	
$Nd_{50}La_{50}$	9.0	4.4	8.5	
$Nd_{65}La_{35}$	5.8	3.2	6.0	

The values of the paramagnetic ordering temperature do not correlate

very well with the values of the Néel temperature. This may be expected if the nature of the magnetic ordering changes as the alloy concentration is changed. The values of the effective moment are fairly close to the expected theoretical value of 3.68 μ_B per Nd atom. This indicates that there are probably no valence changes on the Nd ions in this alloy system.

The low temperature anomalies found in each measurement (electrical resistivity, thermoelectric power and magnetic susceptibility) are shown as a function of the La concentration of the alloys in Figure 14. The top solid line shows the nearly linear decrease of the Néel temperature as the La concentration is increased. The bottom solid line outlines the variation of the second anomaly in the resistivity and susceptibility measurements. These two measurements correlate well. The low temperature anomaly has a minimum at 20% La and then rises in temperature until it merges with the Néel temperature line at 50% La. If this bottom line does correspond to a magnetic ordering phenomenon, then it is probable that the magnetic structure is different in the three regions: $x<20\%$, $20\% \leq x \leq 50\%$, $x>50\%$, where x is the La concentration.

However, the thermoelectric power results cast doubt on the above interpretation. Additional anomalies are seen in S(T) in Figure 14 which do not correlate with the resistivity and susceptibility results. Furthermore there seems to be no consistent trend of the thermopower data. There are probably other features present in some of the alloys which were not large enough to be detected by the equipment which was used. Comparison with other experiments and interpretation of the

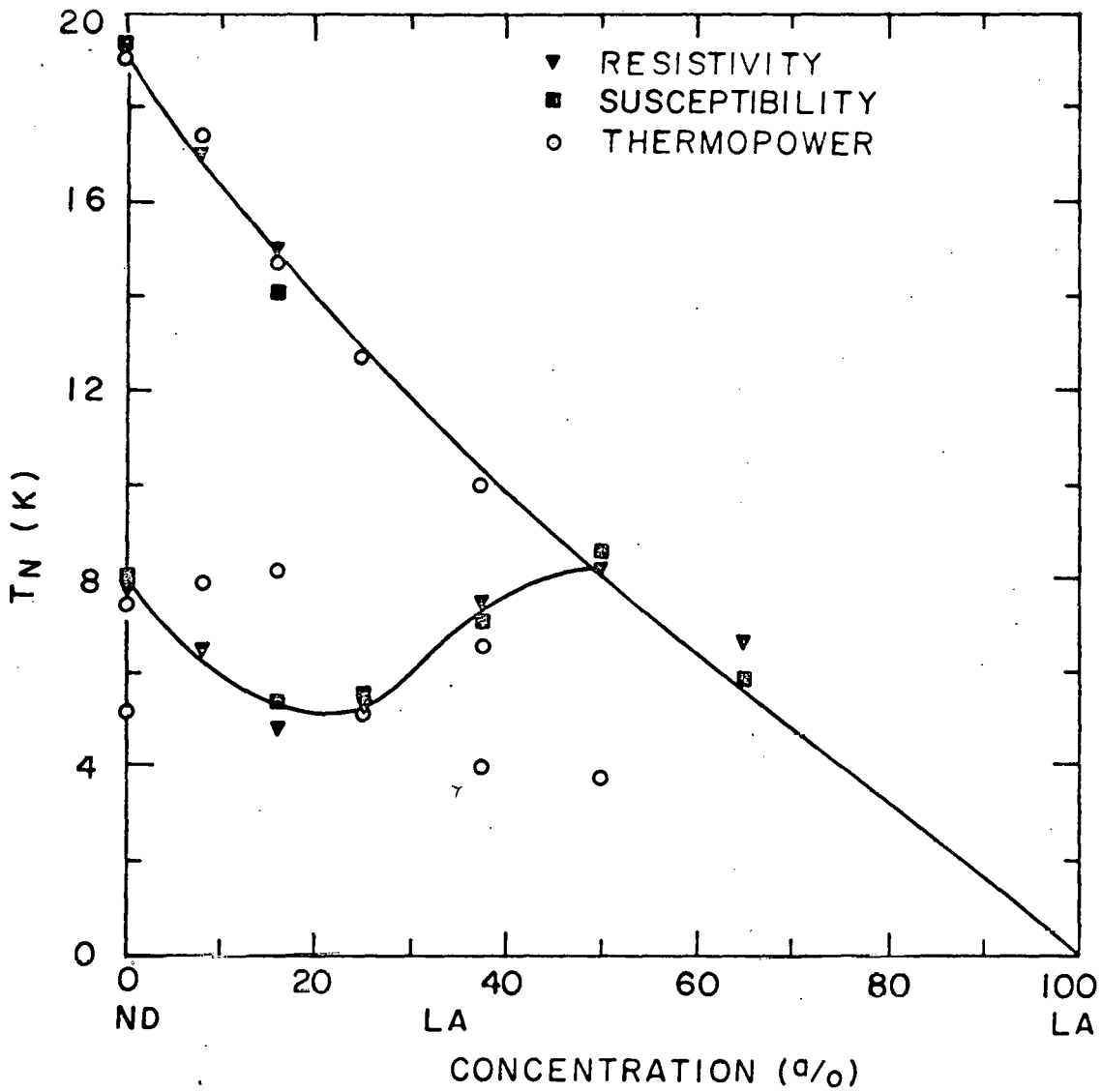

Figure 14. Magnetic ordering features in measurements on Nd-La alloys

nature of the anomalies will be done in the next chapter.

B. Ce-La Alloys

The electrical resistivity of some of the polycrystalline dhcp Ce-La alloys is shown in Figure 15. Also shown is published data on dhcp Ce (6) and La (62). The room temperature resistivity decreases monotonically as a function of the La concentration. However the Debye temperatures (147K for Ce and 142K for La, 63) and the ionic masses (140 for Ce and 139 for La) are nearly identical so that the phonon contribution should be nearly independent of the concentration of the Ce-La alloys. The additional resistivity of the Ce rich alloys must be almost entirely from magnetic scattering processes, e.g., spin disorder scattering and Kondo scattering. Below the magnetic ordering temperature these processes are not allowed because the magnetic moments become "frozen in" to the periodicity of the magnetic arrangement. This accounts for the sudden drop off of the resistivity of the Ce-La alloys at low temperatures.

There are also changes in the slope of the resistivity at the magnetic ordering temperatures as in the Nd-La alloys. Figure 16 shows these effects in the electrical resistivity of the $Ce_{30}La_{70}$ alloy. The second derivative, $d^2\rho/dT^2$, is computed in the same manner as described previously. The negative peaks in the plot of $d^2\rho/dT^2$ correlate well with the points of intersection of straight lines drawn through the resistivity data. The temperatures obtained by the graphical method and numerical method usually agree to within 0.2K. Some exceptions are when only two anomalies are seen by the graphical method but three are

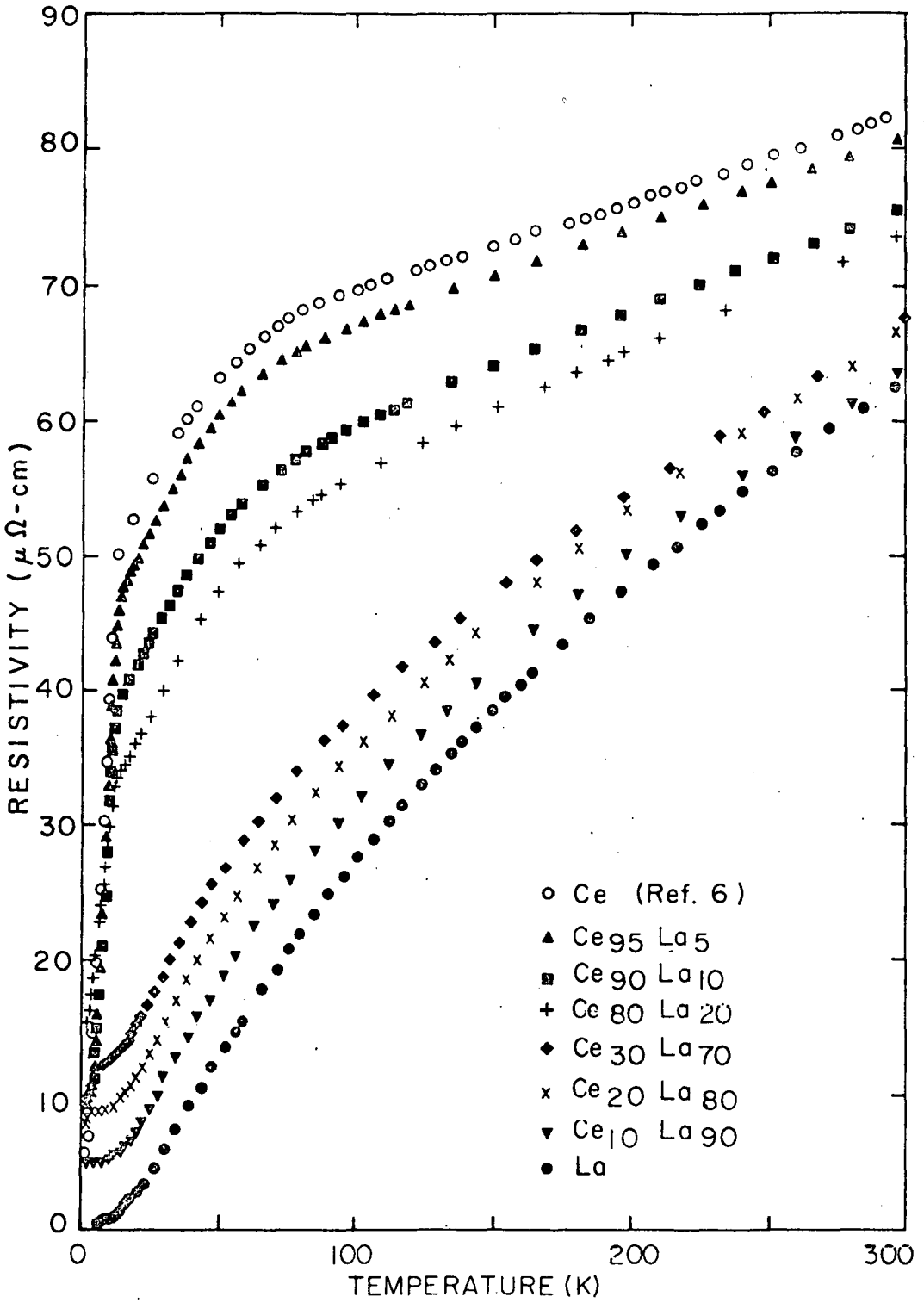

Figure 15. Electrical resistivity versus temperature of Ce-La alloys

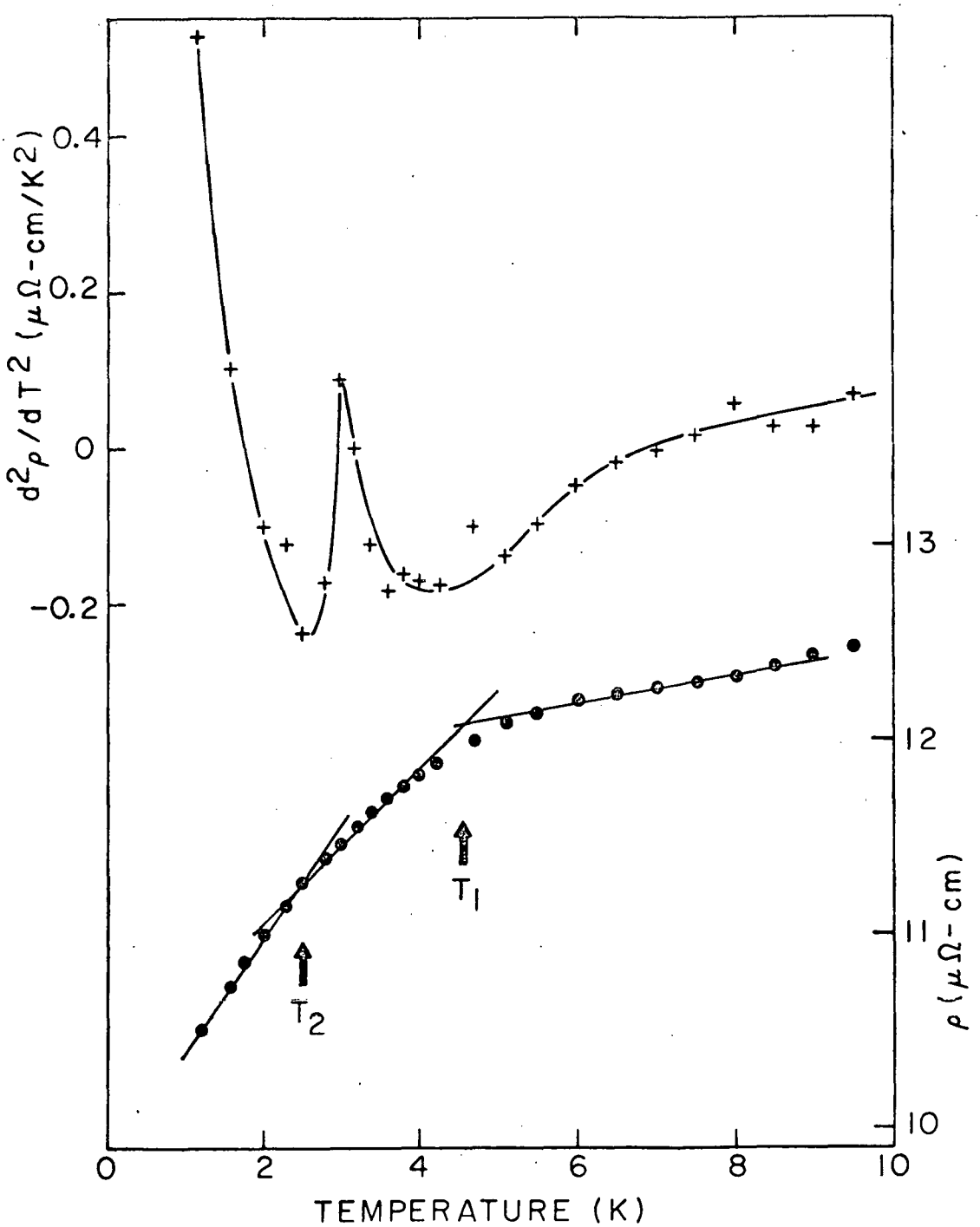

Figure 16. Low temperature electrical resistivity, $\rho(T)$, and $d^2\rho/dT^2$ of $Ce_{30}La_{70}$

obtained numerically, as illustrated in Figure 17. In cases like this the temperatures obtained by the numerical method are used since they correlate better with the effects seen in the heat capacity of these same alloys. There are always at least two anomalies in the Ce-La alloys but never more than three.

The thermoelectric power, S, of dhcp La and Ce-La alloys is shown in Figure 18. At room temperature there is a monotonic decrease in S as a function of concentration. Recalling that the electrical resistivity, ρ, shows the same monotonic decrease, a Gorter-Nordheim plot (S versus $1/\rho$) of this system at room temperature would have a negative slope. This gives unrealistic values to the parameters in the Gorter-Nordheim relation. The reason that this analysis does not work in this system is that a plot of S versus $1/\rho$ requires that only diffusion thermopower be present. It is clear that there are magnetic effects even at room temperature.

All of the samples containing Ce show a positive peak at 70K. The size of this peak is directly related to the Ce concentration but the temperature of the peak is not sensitive to this. The thermopower changes sign at lower temperatures. There is a rather sharp negative peak in the Ce alloys which changes size and temperature as a function of concentration. The shape of this effect is very similar to the Kondo effect seen in the Cu wire with Fe impurities, Figure 7. However, this effect occurs below the Néel temperatures of the $Ce_{95}La_5$ and $Ce_{78}La_{22}$ alloys. If the peaks are due to Kondo-like effects, they would have been affected by the competing effect of magnetic ordering.

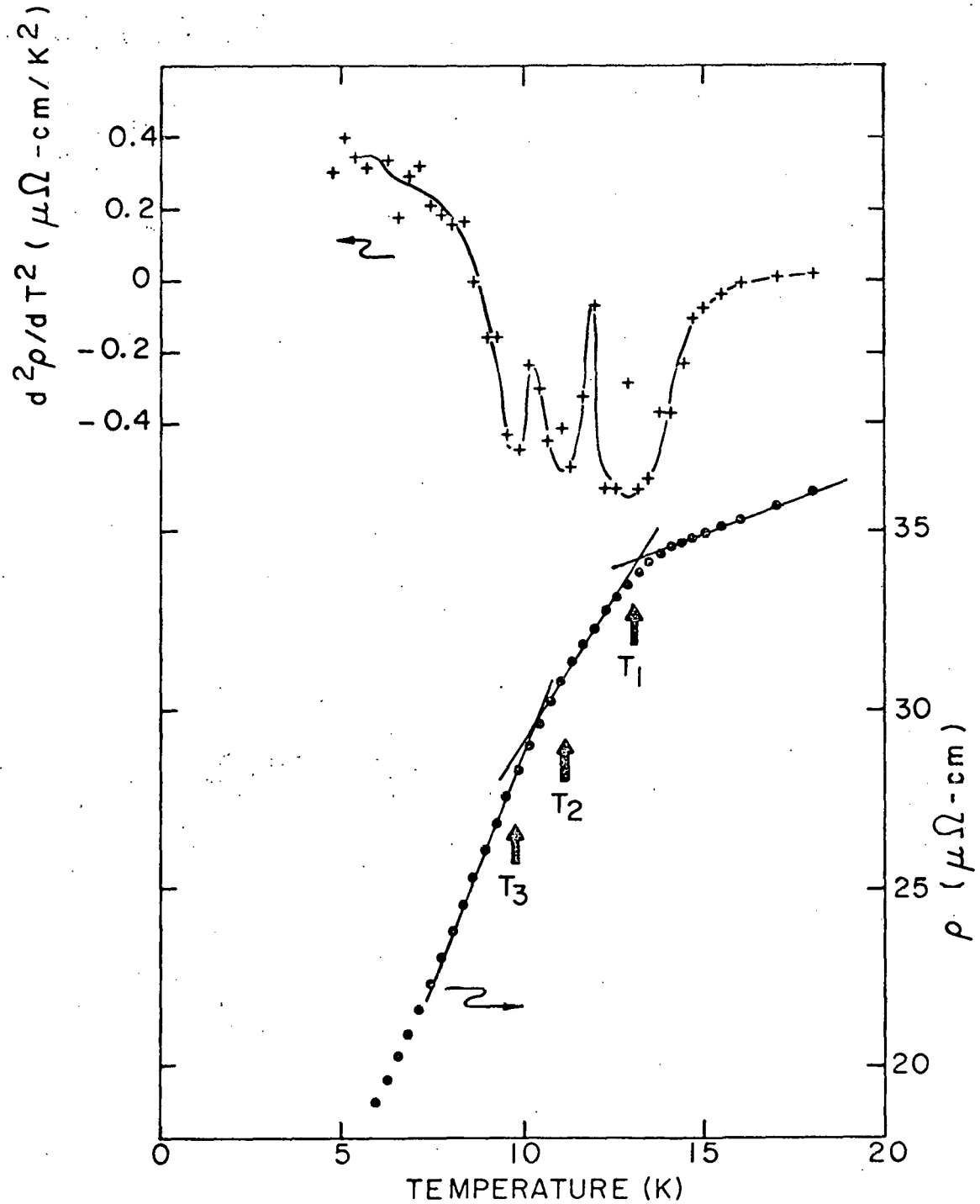

Figure 17. Low temperature electrical resistivity, $\rho(T)$, and $d^2\rho/dT^2$ of $Ce_{78}La_{22}$

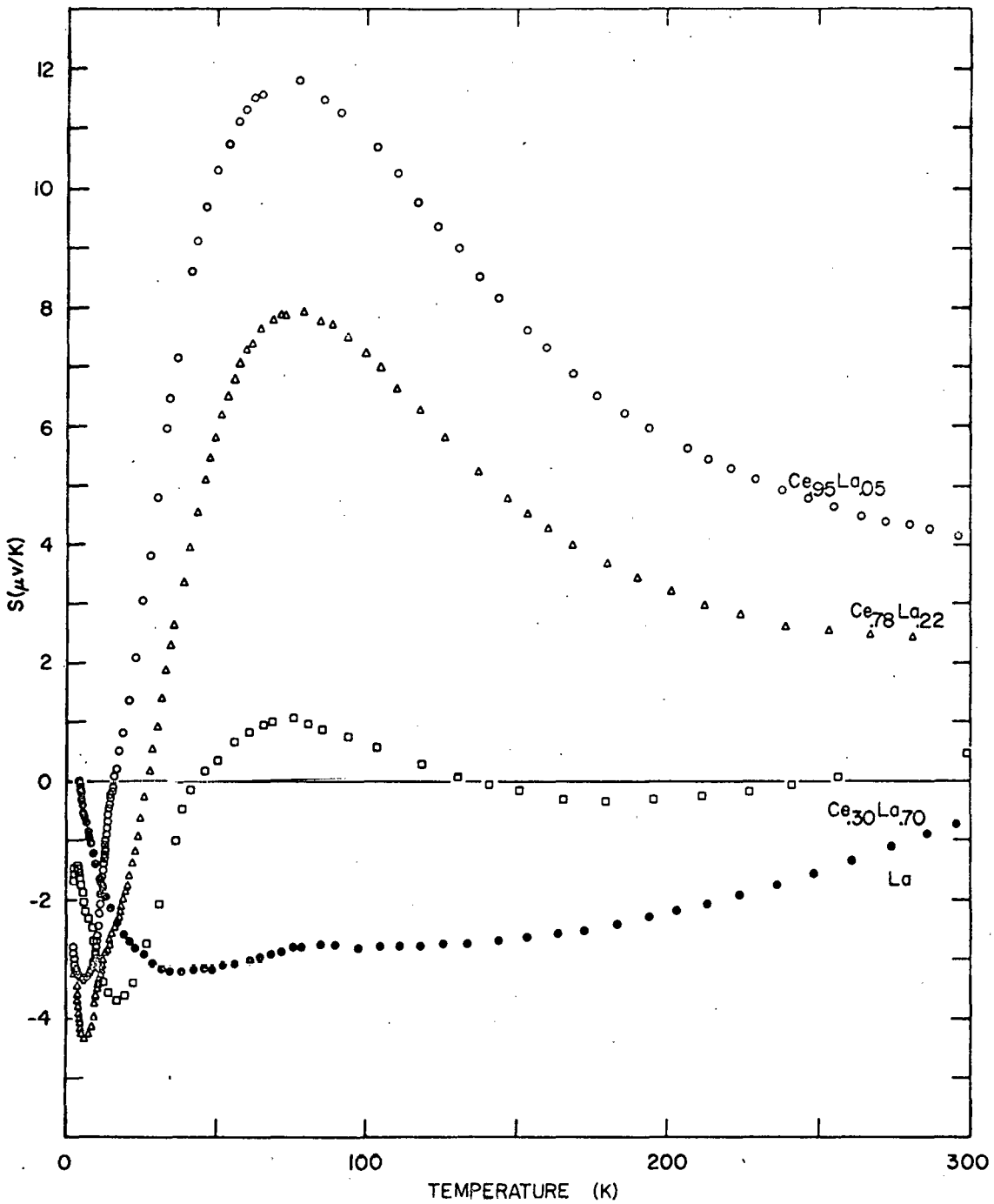

Figure 18. Thermoelectric power of Ce-La alloys

Another possible explanation for these peaks is phonon drag. This can be ruled out, however. The temperature of the phonon drag peak is primarily dependent on the Debye temperature. The Debye temperature of the Ce-La alloys should not be a strong function of concentration. Hence the phonon drag peak of the Ce-La alloys should be about the same as for pure La. Figure 19 shows the thermopower of dhcp and fcc La. The phonon drag peak is clearly evident at about 30K in each sample. These peaks are also much wider than the low temperature peaks in the Ce-La alloys.

The thermopower of the Ce-La alloys also showed a change of slope at the Néel temperatures. It was a very small effect in this system also and it was difficult to resolve the double and triple anomalies.

The magnetization of these alloys is measured at low temperatures at constant applied field. The susceptibility shows a cusp at the Néel temperature which is broadened by the presence of the other anomalies. These can not be resolved if they are less than 2K apart. The VSM is rather inadequate for doing these measurements on antiferromagnetic light rare earth metals. The sample signal is proportional to the amount of magnetic material in the sample. With samples with high La concentration it is hard to get a large enough signal without going to excessively high applied magnetic fields.

Figure 20 shows the inverse susceptibility of some of the Ce-rich alloys. These are particularly good in exhibiting Curie-Weiss behavior. The cusps near 12K are the Néel temperatures. A summary of the magnetic data on the Ce-La alloys is given in Table 2.

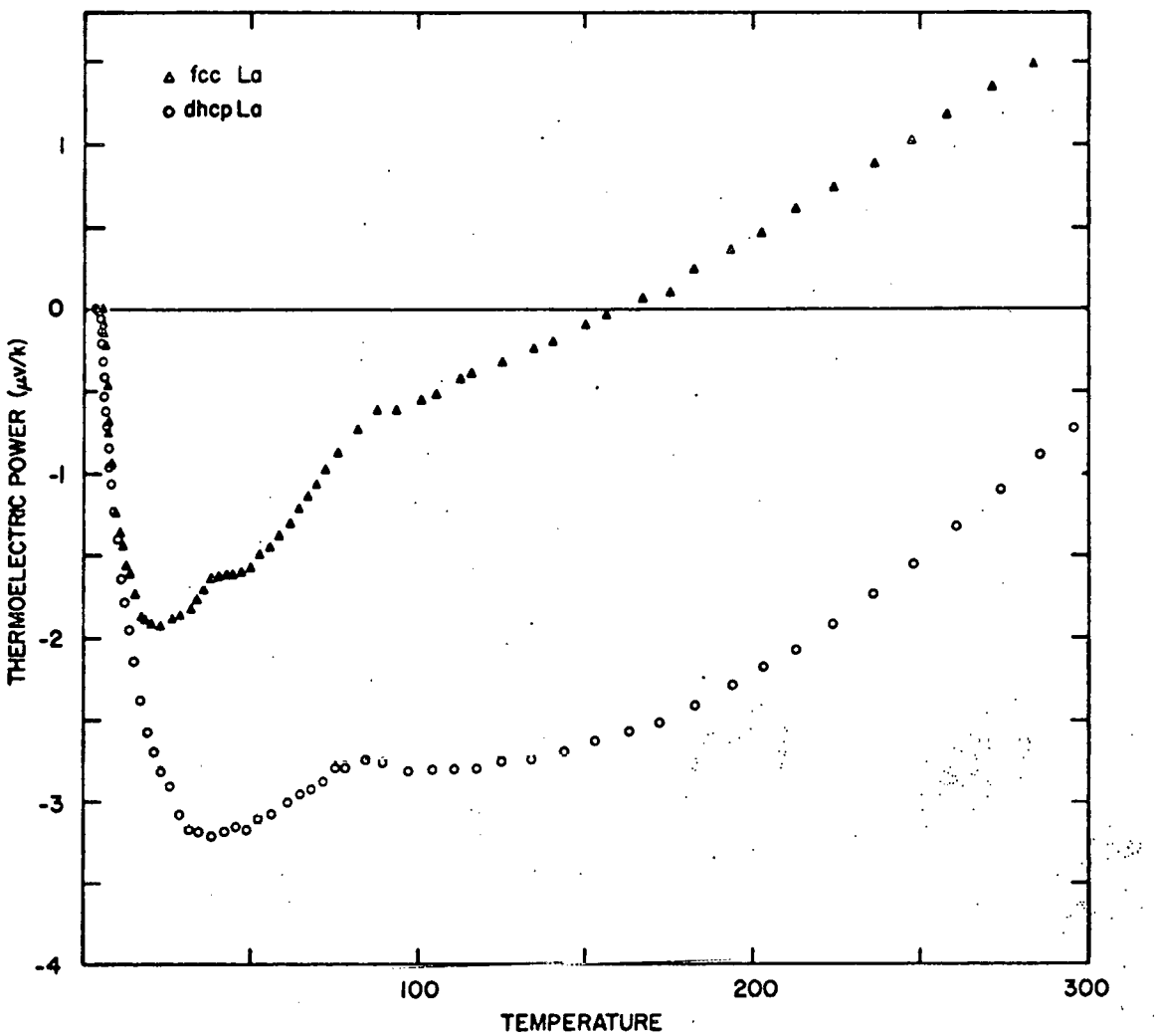

Figure 19. Thermoelectric power of polycrystalline dhcp and fcc La

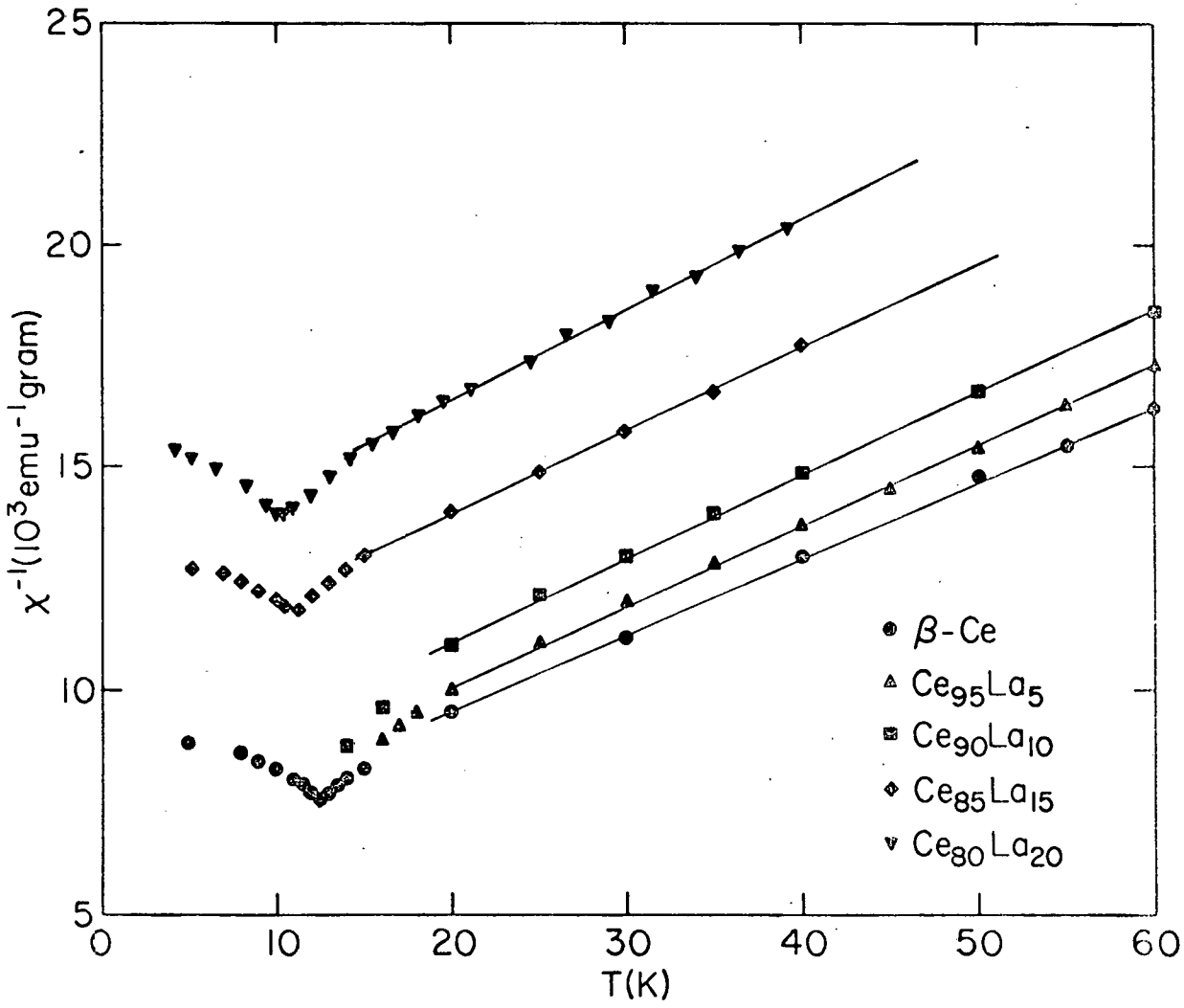

Figure 20. Inverse susceptibility versus temperature of Ce-La alloys and β-Ce (Ref. 6)

Table 2. Magnetic parameters of Ce and Ce-La alloys

Alloy	θ_p(K)	μ_{eff}(μ_B/atom Ce)	T_N(K)	Reference
β-Ce	-38	2.60	12.7	66
$Ce_{95}La_5$	-40	2.55	12.1	
$Ce_{90}La_{10}$	-45	2.50	11.2	
$Ce_{85}La_{15}$	-56	2.46	10.8	
$Ce_{80}La_{20}$	-58	2.34	10.2	
$Ce_{66}La_{34}$	5.9	2.67	8.0	
$Ce_{48}La_{52}$	3.0	3.41	5.5	
La	-216	0.58		67

The effective magnetic moments are in good agreement with the theoretical value of $2.54\mu_B$ per Ce atom. Hence the Ce ions remain in the $4f^1$ configuration. The two alloys $Ce_{66}La_{34}$ and $Ce_{48}La_{52}$ have effective moments which are too high and paramagnetic ordering temperatures which are not consistent with the other alloys. An explanation, to be discussed in the next chapter, is that these intermediate concentration alloys have considerable fcc contamination. Also the experimental error increases with reduced Ce concentration.

The low temperature magnetic effects are summarized in Figure 21. The temperature of the effects in the resistivity, susceptibility, and the heat capacity measurements of Tsang and Gschneidner (68) are plotted versus the La concentration of the alloys. All of the alloys show at least two distinct features and those with less than 40% La have three. The heat capacity is the most sensitive measurement of these effects. Peaks occur at the temperatures indicated except when

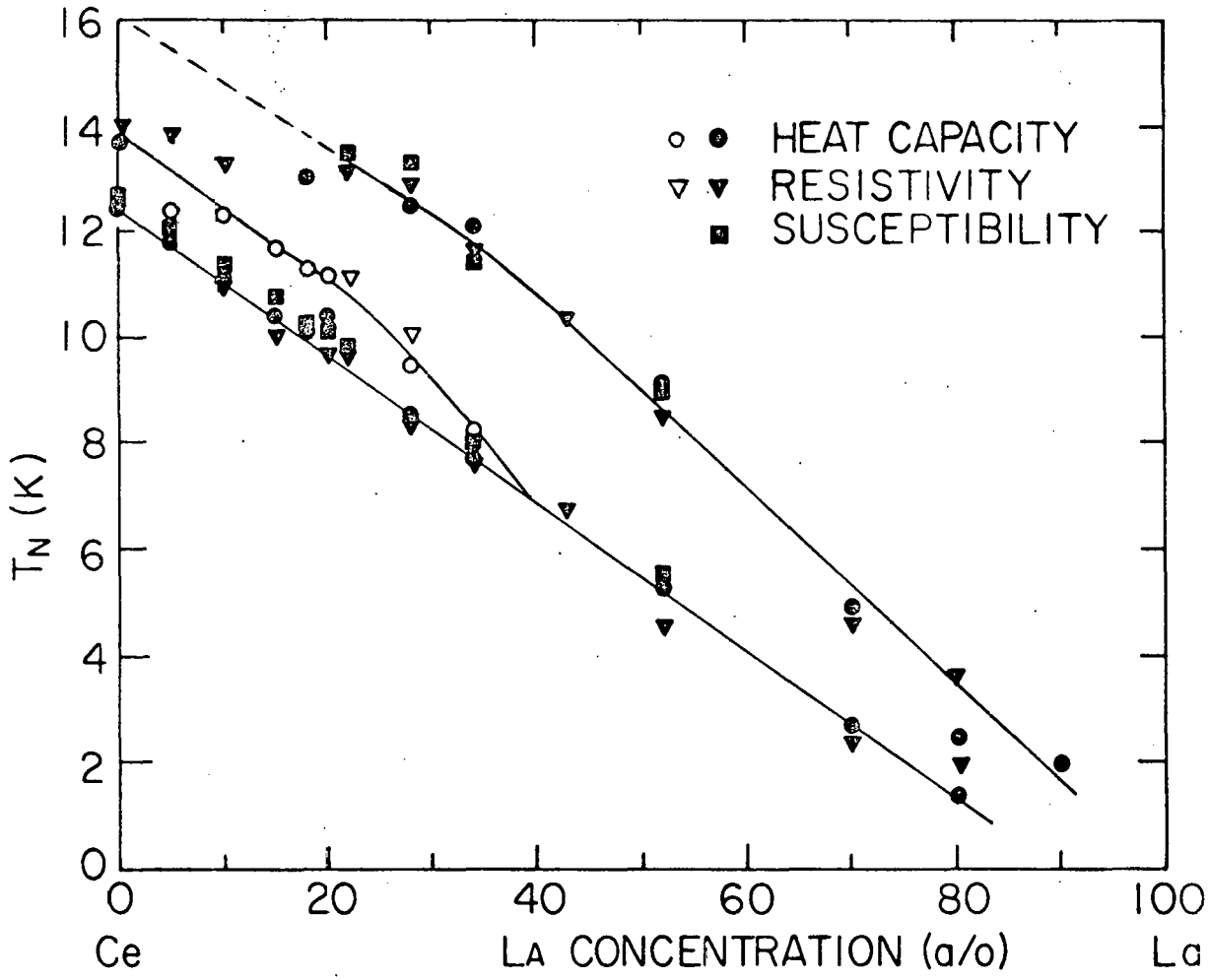

Figure 21. Magnetic ordering features in measurements on Ce-La alloys (heat capacity data of Tsang and Gschneidner (Ref. 68))

they are close enough together to make a single peak with a shoulder. The thermoelectric measurements on Ce-La alloys are consistent with Figure 21 but are not as sensitive as these other measurements.

V. DISCUSSION

A. Magnetic Ordering Phenomena

Since the nature of the magnetic order in Nd itself is not fully understood, it is impossible to determine the exact nature of all of the susceptibility and transport anomalies in the Nd-La alloys of Figure 14. However, comparisons may be made with the available neutron diffraction and heat capacity data.

According to Moon, Cable and Koehler (24), at the Néel temperature of Nd (T_N = 19K) the magnetic moments of the hexagonal (B and C) sites of the dhcp lattice are periodic with an amplitude ($\mu_{hex} = 2.3 \pm 0.2\mu_B$) which is somewhat less than the expected saturation moment of Nd ($gJ = 3.27\mu_B$). Bak and Lebech (13) have estimated that the moments of the cubic (A) sites have an amplitude of only 10-20% of the hexagonal sites. At 7.5K the amplitude of the cubic site moments suddenly grows to $\mu_{cub} = 1.8 \pm 0.2\mu_B$ (24). Also near 7.5K the wave vector of the magnetic order reaches the commensurate value of 0.125 b_1, where b_1 is a reciprocal lattice vector.

The wave vector of the magnetic order is determined by the spacing of magnetic satellite peaks from the reciprocal lattice peaks. Lebech and Rainford (69) have found that these satellites show anomalous behavior. Near 8K each of the cubic site satellites actually has three closely spaced components. This splitting disappears below 7K. Below 6.5K the hexagonal site satellites split into components giving magnetic wave vectors which differ as much as 8%. This splitting disappears at 4.2K if a magnetic field greater than 8kOe is applied.

The heat capacity of electrotransported Nd, measured by Forgan et al. (15), is shown in Figure 22. In an applied magnetic field of 2.8 kOe there are five distinct peaks in $C_p(T)$ between 5 and 8K. The interpretation of Forgan et al. is that the two highest peaks (7.8 and 8.3K) are due to magnetic ordering on the cubic sites, e.g., the sudden increase in the cubic site moments and the appearance and disappearance of the splitting of the cubic site satellites. The amplitudes and temperatures of the two peaks between 5 and 6K are sample dependent and also are dependent on the thermal history of the sample, i.e., the peaks shift when data are taken during cooling or warming. These peaks are thought to be associated with the splitting seen in the hexagonal site satellites. Possible explanations are (i) magnetic domain effects and (ii) interaction between cubic site and hexagonal site magnetic moments (70).

The electrical resistivity of c-axis Nd shows evidence in Figure 9 of a double anomaly at 7.3 and 8.0K. These probably correspond to the heat capacity peaks at 7.8 and 8.3K. The resistivity also shows a change of slope at 5.8K which probably is associated with the heat capacity peak in the same vicinity (5.8K during cooling, 6.3K during warming). The resistivity of all of the Nd-La alloys was measured from 1.2 to 30K during warming only.

The thermoelectric power of Nd also shows small anomalies at 5.1K and 7.5K. The data shown in Figure 12 were all taken during warming only. Some data were taken while cooling and temperature hysteresis was observed near 5K. The cooling data was slightly higher than the

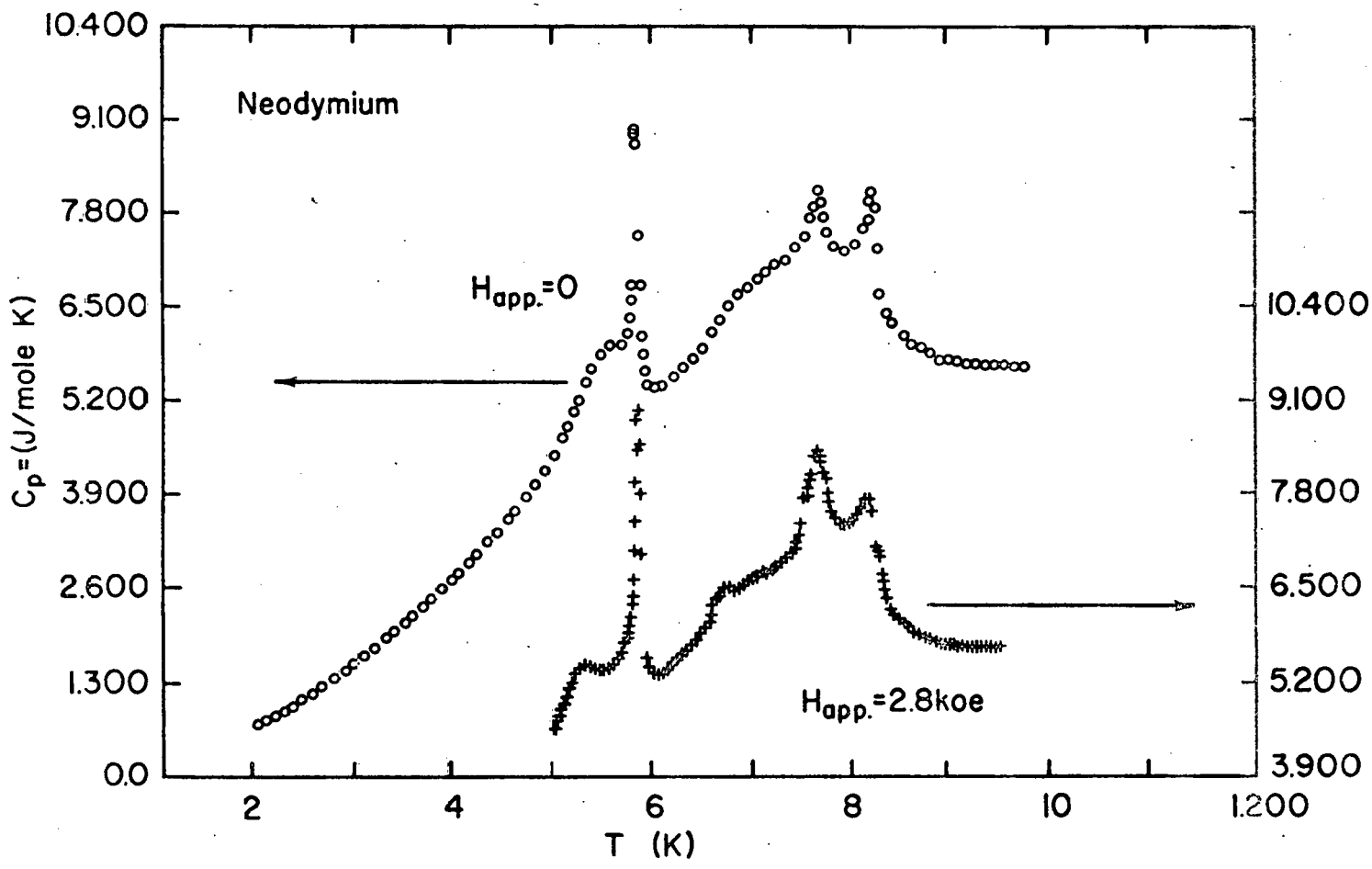

Figure 22. Heat capacity of polycrystalline Nd, Forgan et al. (15)

warming data. Also, at a fixed temperature the thermoelectric power would drift upwards over a period of several hours.

If the interpretation is correct that some of the heat capacity and neutron diffraction effects are magnetic domain effects, then the scatter seen in Figure 14 may be partially attributed to sample dependent domain effects. These are polycrystalline alloys so that there may be regions of preferred crystalline orientation, although x-ray results indicate that this is not the case.

The upper line of Figure 14 is the Néel temperature line. The neutron diffraction results on Nd indicate that this is primarily an ordering on the hexagonal sites. The lower line is then due to the sudden increase in the moments on the cubic sites. The merging of the two lines at 50% indicates that the distinction between the two kinds of sites may have disappeared because of the La dilution.

The magnetic order of β-cerium is less well-understood than neodymium. Neutron diffraction on polycrystalline β-Ce shows an antiferromagnetic structure at 12.5K (71). Definitive results on the direction and nature of the magnetic order and size of the moments cannot be obtained without using single crystals. The heat capacity of β-Ce, measured by Koskimaki and Gschneidner (5), shows two peaks located at 12.45K and 13.7K. They postulate that both peaks are due to magnetic ordering effects, perhaps distinct orderings on the hexagonal sites and on the cubic sites as in neodymium. The relative size of the heat capacity peaks as well as the $d^2\rho/dT^2$ peaks vary with the La concentration of the alloy. For alloys with La concentrations in the

range 20-70%, the highest temperature peaks shown in Figure 21 are the largest. X-ray photographs of these alloys reveal a large amount of the fcc phase in the sample, perhaps 50% or more judging by the relative intensity of the x-ray spots from the dhcp and fcc phases. All of the other alloys show little fcc contamination and the highest temperature heat capacity peaks are diminished also. The residual resistivity is also affected by the presence of the fcc phase. As shown in Figure 23, the residual resistivity of the Nd-La alloys is well-behaved and follows the Nordheim rule, Equation 15. However, the residual resistivity of the Ce-La alloys drops suddenly near 20% La indicating that fcc is present. The starting metals, Ce, La and Nd, used for these alloys were of about equal purity so that the variation of the residual resistivity cannot be attributed to impurity effects.

The temperature hysteresis observed in measurements on β-Ce is caused by the phase changes of $\beta \rightarrow \alpha$ during cooling and $\alpha \rightarrow \gamma$ upon warming. The phase diagram of Gschneidner et al. (72) indicates that the α phase should no longer be present in Ce-La alloys with 5% or more La. In fact, there is no temperature hysteresis in the resistivity of these alloys if there is more than 2% La present. It appears that the β and γ phases of Ce-La alloys with 20-70% La coexist at temperatures from 300K to 1.2K.

It is clear that the upper line of Figure 21 must be the magnetic ordering of the fcc phase. The two lower lines which merge into one at 40% La may be ordering on the hexagonal and cubic sites of the dhcp phase as in the case of Nd. This double anomaly is observed in every

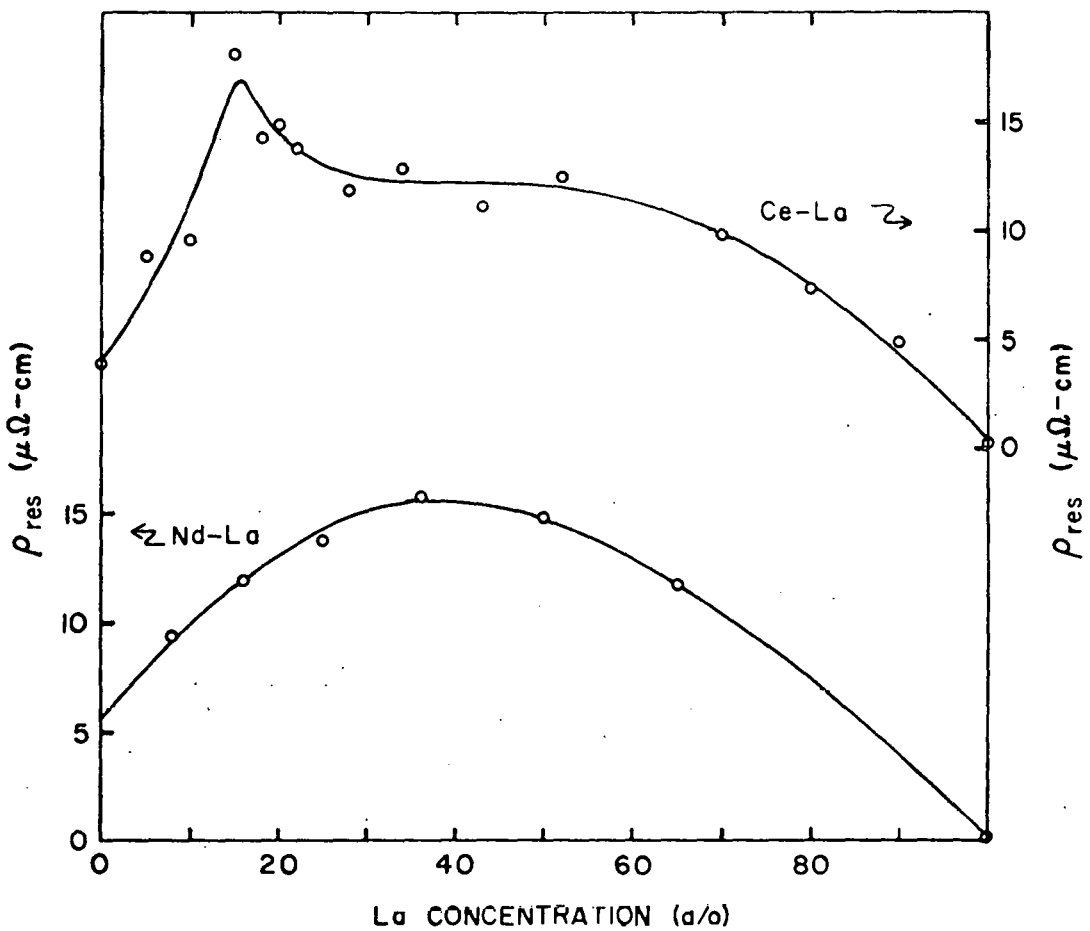

Figure 23. Residual resistivity ($\rho_{1.2K}$) of Ce-La and Nd-La alloys

heat capacity sample and in several of the resistivity measurements.

Other proposed explanations of the heat capacity peaks include Schottky effects and Kondo effects. However these peaks cannot be Schottky peaks because (i) the temperature dependence of the peaks cannot be fit with reasonable crystal field parameters and (ii) they would not be manifested as abrupt changes of slope in the resistivity measurements. Kondo effects are seen in the resistivity as discussed in the next section, but they are manifested at higher temperatures and do not cause abrupt changes in the slope of the resistivity.

B. Kondo Effect in Ce-La Alloys

The Kondo effect has generally been considered a dilute magnetic alloy phenomenon because the derivation of the Kondo effect assumes that the localized magnetic moments are noninteracting. In particular, the coupling of the local moment to the conduction electrons must be much greater than the coupling to nearby moments, thus allowing the local moment the freedom to exchange spin with the conduction electrons.

The close proximity of the 4f electron to the Fermi level in Ce and Ce-La alloys results in a strong Kondo interaction between the 4f moments and the conduction electrons. In β-Ce the Kondo resistivity anomaly appears at temperatures well above T_N where the 4f moments are uncorrelated. Kondo effects seen in Ce-La alloys include (i) $\chi \sim T^{-1/2}$ for La-rich alloys (73) and (ii) a minimum in the electrical resistivity for La concentrations from 14 to 20% (10, 74).

Several theories have been proposed which can explain these Kondo effects. In the Kondo sideband models (45, 46) and related crystal

field models (12), Kondo scattering can occur when the temperature is high enough to populate excited crystal field levels. These theories neglect 4f-4f interaction effects and one would expect these to work only for dilute alloys. In spite of this, very good fits can be made to experimental data on the susceptibility, resistivity, and thermoelectric power of nondilute Ce compounds and alloys. The crystal field parameters obtained in these fits to different experiments seldom agree with each other and can vary by factors of 3 or 4.

Other theories (11, 75) have approximated the 4f-4f interaction with a mean internal field, H. The ln T term in the resistivity is then modified to the form

$$\rho_k \sim \ln(T^2 + T_H^2)^{1/2} \tag{60}$$

where $T_H = H/k_B$ is used as a fitting parameter.

Figure 24 shows the magnetic part of the electrical resistivity of Ce-La alloys. This is computed by subtracting the resistivity of dhcp La (62) which should be a good approximation to the phonon resistivity of the alloy. The residual resistivity of each alloy is also subtracted so that

$$\rho_{mag}(T) = \rho(T) - \rho_{La}(T) - \rho(1.2K) \ . \tag{61}$$

The solid line drawn through the pure Ce data is a computer fit to the model of Liu et al. (11). Well above $T_N = 13.7K$, ρ_{mag} has the temperature dependence of Equation 60. As the temperature approaches T_N, the Kondo resistivity gets quenched because the spin-flip processes are frozen out by short range ordering of the local moments. This

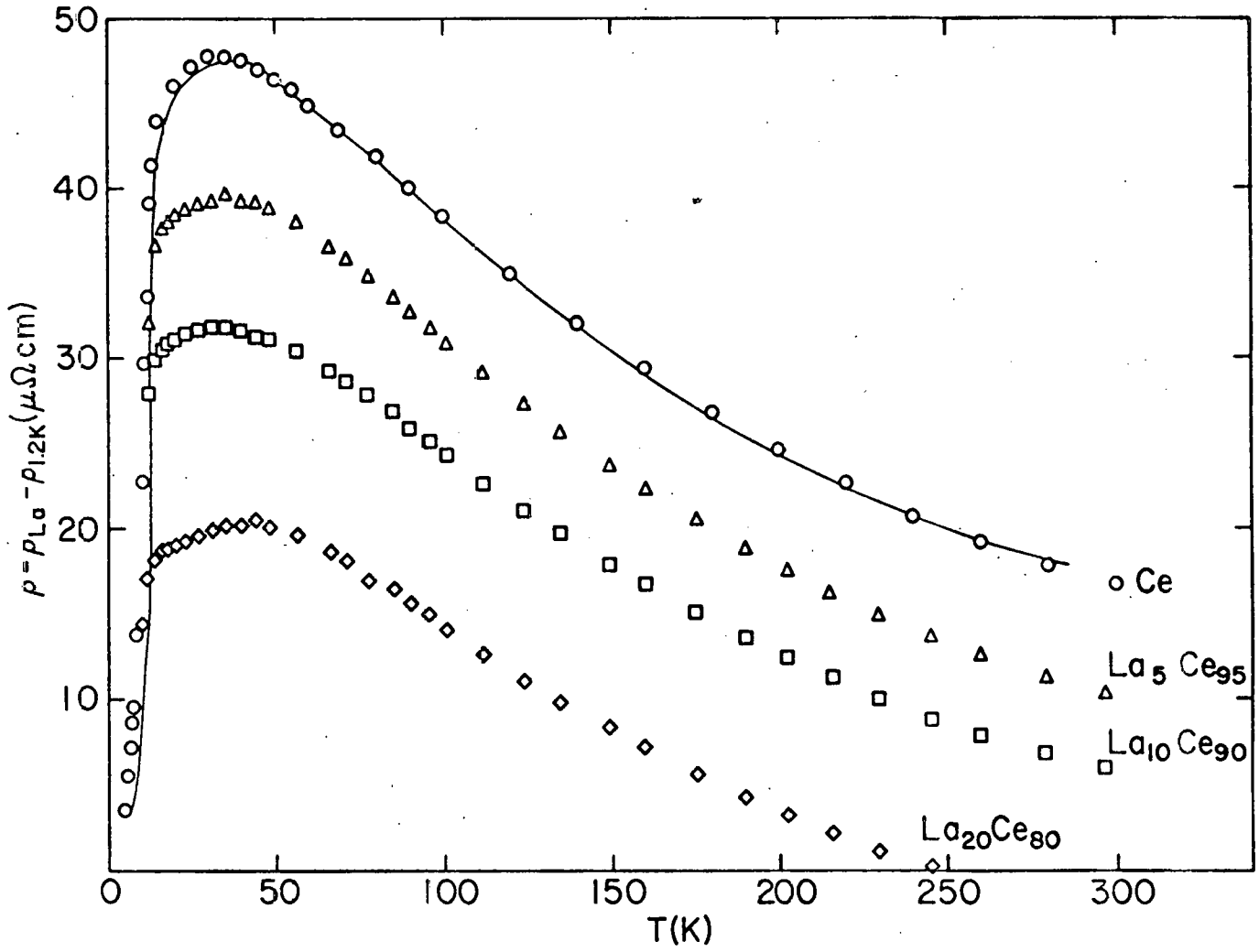

Figure 24. Magnetic part of the electrical resistivity of Ce-La alloys

theory works well for all of the Ce-La alloys.

The crystal field theories may also be used to fit the data of Figure 24, but the resultant crystal field splitting is much too low. In general these models predict a peak in the resistivity at a temperature equal to the crystal field splitting. The peak in the resistivity occurs near 30K while the measured crystal field splittings are 98K and 113K for the hexagonal sites and 206K for the cubic sites of Ce ions (6).

The Kondo effect is manifested in the thermoelectric power as a low temperature peak near the Kondo temperature. Bhattacharjee and Coqblin (52) have modeled the thermoelectric power of Ce compounds and alloys with a theory based on resonant Kondo scattering from excited crystal field levels. This model is described in Appendix A and predicts a peak in the thermopower at a temperature between 1/6 and 1/3 of the crystal field splitting. The magnetic part of the thermopower of $Ce_{95}La_5$ shown in Figure 25 is obtained by subtracting the phonon contribution to the thermopower. This is approximated by the thermopower of La. The best fit to the magnetic thermopower using the theory of Bhattacharjee and Coqblin is shown by the solid line in Figure 25. This fit uses the known crystal field splittings and achieves a good result considering the complexity of the phenomenon. The temperature and size of the peak are approximated well, but the temperature dependence is not exactly right. The local moment--conduction electron exchange coupling constant is approximately -0.4 eV which is the correct sign and order of magnitude for Ce. This theory

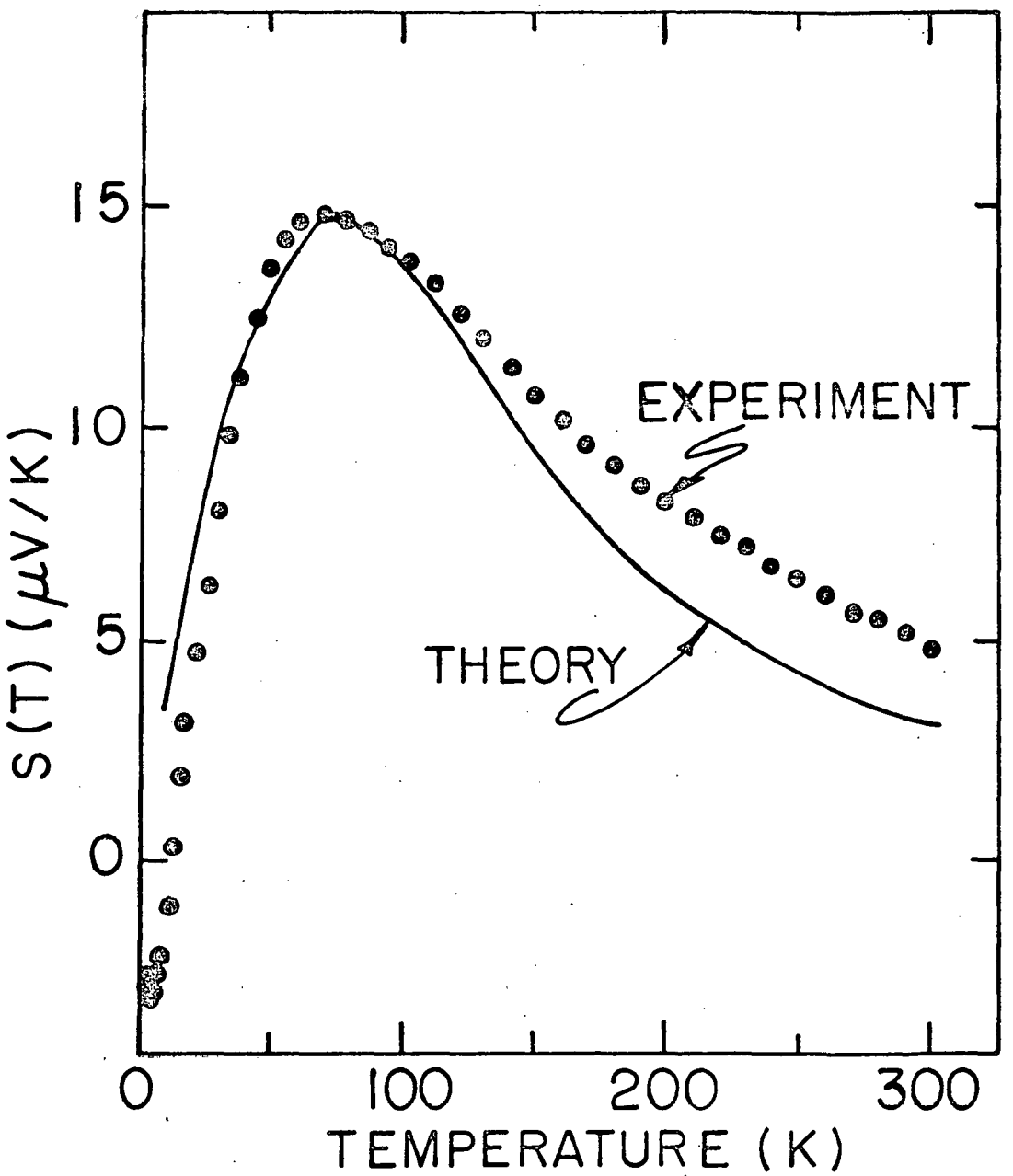

Figure 25. Magnetic part of the thermopower of $Ce_{95}La_5$ alloy

neglects 4f-4f interactions and it is expected that a theory incorporating these along with crystal field effects would give very good results.

VI. SUMMARY

The electrical resistivity, thermoelectric power and magnetic susceptibility on neodymium single crystals and polycrystalline dhcp Nd-La and Ce-La alloys have been measured at low temperatures. The measurements on the Nd-La alloys show features at the Néel temperatures and also show additional magnetic ordering phenomena. Some of these other features are dependent on the thermal history of the sample. Magnetic field studies are needed to correlate these features with observed neutron diffraction effects.

Several magnetic features are seen in the Ce-La alloy system also, although the measurements are plagued with the problem of fcc contamination. In addition, alloys containing Ce show Kondo effects. The logarithmic term in the resistivity is explained well by the theory of Liu et al. (11) which uses a mean field to approximate the 4f-4f interactions in the nondilute alloys. The large peak in the thermopower of Ce-La alloys is explained well by the theory of Bhattacharjee and Coqblin (52) which incorporates Kondo scattering from excited crystal field levels.

VII. BIBLIOGRAPHY

1. O. D. McMasters, G. E. Holland, and K. A. Gschneidner, Jr., J. Cryst. Growth 43, 577 (1978).

2. P. G. Mattocks, C. M. Muirhead, D. W. Jones, B. J. Beaudry, and K. A. Gschneidner, Jr., J. Less Common Met. 53, 253 (1977).

3. D. C. Koskimaki, K. A. Gschneidner, Jr., and N. T. Panousis, J. Cryst. Growth 22, 225 (1974).

4. F. Trombe and M. Foex, C. R. Acad. Sci. (Paris) 217, 501 (1943).

5. D. C. Koskimaki and K. A. Gschneidner, Jr., Phys. Rev. B 10, 2055 (1974).

6. P. Burgardt, K. A. Gschneidner, Jr., D. C. Koskimaki, D. K. Finnemore, J. O. Moorman, S. Legvold, C. Stassis, and T. A. Vyrostek, Phys. Rev. B 14, 2997 (1976).

7. M. K. Wilkinson, H. R. Child, C. J. McHargue, W. C. Koehler, and E. O. Wollan, Phys. Rev. 122, 1409 (1961).

8. L. M. Roberts and J. M. Lock, Phil. Mag. 2, 811 (1957).

9. R. O. Elliott, H. H. Hill, and W. N. Miner, Phys. Stat. Sol. 32, 609 (1969).

10. A. S. Edelstein, Phys. Lett. 27A, 614 (1968).

11. S. H. Liu, P. Burgardt, K. A. Gschneidner, Jr., and S. Legvold, J. Phys. F 6, L55 (1976).

12. B. Cornut and B. Coqblin, Phys. Rev. B 5, 4541 (1972).

13. P. Bak and B. Lebech, Phys. Rev. Lett. 40, 800 (1978).

14. R. M. Moon, W. C. Koehler, C. Stassis, G. R. Kline, and S. K. Sinha, Proc. Int. Conf. Mag., (to be published 1979).

15. E. M. Forgan, C. M. Muirhead, D. W. Jones, B. J. Beaudry, and K. A. Gschneidner, Jr., J. Phys. F, (to be published 1979).

16. W. C. Koehler, Magnetic structures of rare earth metals and alloys, in Magnetic properties of rare earth metals, edited by R. J. Elliott (Plenum Press, New York, 1972).

17. J. M. Lock, Phil. Mag. 2, 726 (1957).

18. M. V. Vedernikov, I. A. Markova, and G. N. Meshkova, Sov. Phys. Sol. State 7, 766 (1965).

19. S. D. Grobman, J. Appl. Phys. 42, 1456 (1971).

20. H. J. Born, S. Legvold, and F. H. Spedding, J. Appl. Phys. 32, 2543 (1961).

21. K. W. H. Stevens, Proc. Phys. Soc. A65, 209 (1952).

22. W. E. Wallace, Rare earth intermetallics (Academic Press, New York, 1973).

23. O. V. Lounasmaa and L. J. Sundström, Phys. Rev. 158, 591 (1967).

24. R. M. Moon, J. W. Cable, and W. C. Koehler, J. Appl. Phys. Suppl. 35, 1041 (1964).

25. B. Lebech and B. D. Rainford, J. Phys. (Paris) 32, C1-370 (1971).

26. B. Bleaney, in Proceedings of the third conference on rare earth research, edited by K. S. Vorres (Gordon and Breach, New York, 1963) p. 417.

27. N. T. Panousis, Low temperature specific heat of cerium and cerium-yttrium alloys (unpublished Ph.D. thesis, Library, Iowa State University, Ames, Iowa, 1970).

28. G. S. Fleming, S. H. Liu, and T. L. Loucks, Phys. Rev. Lett. 21, 1524 (1968).

29. J. M. Ziman, Electrons and phonons (Oxford University Press, London, 1960).

30. J. M. Ziman, Principles of the theory of solids (Cambridge University Press, Cambridge, England, 1964).

31. N. F. Mott and H. Jones, The properties of metals and alloys (Dover Publications, New York, 1936).

32. S. Legvold, Transport properties, in Magnetic properties of rare earth metals, edited by R. J. Elliott (Plenum Press, New York, 1972).

33. R. J. Elliott and F. A. Wedgewood, Proc. Phys. Soc. 81, 846 (1963).

34. A. J. Dekker, J. Appl. Phys. 36, 906 (1965).

35. A. R. Mackintosh, Phys. Lett. 4, 140 (1963).

36. Y. Suezaki and H. Mori, Phys. Lett. 28A, 70 (1969).

37. Ö. Rapp, G. Benediktsson, H. U. Åstrom, S. Arajs, and K. V. Rao, Phys. Rev. B. 18, 3665 (1978).

38. S. Alexander, J. S. Helman, and I. Balberg, Phys. Rev. B 13, 304 (1976).

39. T. G. Richard and D. J. W. Geldart, Phys. Rev. B 15, 1502 (1977).

40. J. Kondo, Sol. St. Phys. 23, 183 (1969).

41. K. Matho and M. T. Beal-Monod, Phys. Rev. B 5, 1899 (1972).

42. T. S. Petersen, S. Legvold, K. A. Gschneidner, Jr., T. W. E. Tsang, and J. O. Moorman, J. Appl. Phys. 49, 2115 (1978).

43. J. R. Schrieffer and P. A. Wolff, Phys. Rev. 149, 491 (1966).

44. B. Coqblin and J. R. Schrieffer, Phys. Rev. 185, 847 (1969).

45. F. E. Maranzana, Phys. Rev. Lett. 25, 239 (1970).

46. H. J. Van Daal, F. E. Maranzana, and K. H. J. Buschow, J. Phys. (Paris) Suppl. 32, C1-424 (1971).

47. D. K. C. MacDonald, Thermoelectricity: an introduction to the principles (John Wiley and Sons, New York, 1962).

48. R. D. Barnard, Thermoelectricity in metals and alloys (Halsted Press, New York, 1972).

49. M. Bailyn, Phys. Rev. 126, 2040 (1962).

50. F. J. Blatt, P. A. Schroeder, C. A. Foiles, and D. Greig, Thermoelectric power of metals (Plenum Press, New York, 1976).

51. P. E. Nielsen and P. L. Taylor, Phys. Rev. B 10, 4061 (1974).

52. A. K. Bhattacharjee and B. Coqblin, Phys. Rev. B 13, 3441 (1976).

53. L. R. Sill, Seebeck effect in heavy rare earth single crystals (unpublished Ph.D. thesis, Library, Iowa State University, Ames, Iowa, 1964).

54. D. W. Mellon, Transport properties of Gd-Th, Gd-Mg, and Y-Th alloys (unpublished Ph.D. thesis, Library, Iowa State University, Ames, Iowa, 1970).

55. M. S. Anderson, H. T. King, and C. A. Swenson, Calibration for An-Fe vs. Cu thermocouples, Private communication (1970).

56. L. L. Sparks, R. L. Powell, and W. J. Hall, Cryogenic thermocouple tables, National Bureau of Standards Report No. 9712 (1968).

57. C. F. Eagen, Resistivity and magnetoresistance of dilute solutions of Cr in Cu-Ni alloys (unpublished Ph.D. thesis, Library, Iowa State University, Ames, Iowa, 1972).

58. R. B. Roberts, Phil. Mag. 36, 91 (1977).

59. A. V. Gold, D. K. L. MacDonald, W. B. Pearson, and I. M. Templeton, Phil. Mag. 5, 765 (1960).

60. P. Burgardt, Fermi surface effects in terbium alloys (unpublished Ph.D. thesis, Library, Iowa State University, Ames, Iowa, 1976).

61. L. R. Sill and S. Legvold, Phys. Rev. 137, A1139 (1965).

62. S. Legvold, P. Burgardt, B. J. Beaudry, and K. A. Gschneidner, Jr., Phys. Rev. B 16, 2479 (1977).

63. O. V. Lounsmaa, in Rare Earth Research II, edited by K. S. Vorres (Gordon and Breach, New York, 1964) p. 221.

64. J. M. Lock, Proc. Phys. Soc. B70, 566 (1957).

65. J. J. Rhyne, Bulk magnetic properties, in Magnetic properties of rare earth metals, edited by R. J. Elliott (Plenum Press, New York, 1972).

66. S. Legvold, T. S. Petersen, K. A. Gschneidner, Jr., P. Burgardt, and J. O. Moorman, Physica 86-88B, 55 (1977).

67. F. H. Spedding and J. J. Croat, J. Chem. Phys. 59, 2451 (1973).

68. T.-W. E. Tsang and K. A. Gschneidner, Jr., unpublished information on the heat capacity of the same alloys reported on here.

69. B. Lebech and B. D. Rainford, Proc. 9th Int. Conf. on Magnetism, Moscow, 3, 191 (1974).

70. T. Johansson, B. Lebech, M. Nielsen, H. Bjerrum Møller and A. R. Mackintosh, Phys. Rev. Lett. 25, 524 (1970).

71. M. K. Wilkinson, H. R. Child, C. J. McHargue, W. C. Koehler and E. O. Wollan, Phys. Rev. 122, 1409 (1961).

72. K. A. Gschneidner, Jr., R. O. Elliott and R. R. McDonald, J. Phys. Chem. Sol. 23, 1201 (1962).

73. A. S. Edelstein, Phys. Rev. Lett. 20, 1348 (1968).

74. R. O. Elliott, H. H. Hill and W. N. Miner, Phys. Stat. Sol. 32, 609 (1969).

75. K. Matho and M. T. Beal-Monod, Phys. Rev. B 5, 1899 (1972).

VIII. ACKNOWLEDGEMENTS

My graduate study at Iowa State has been exciting and fruitful. My thanks go to my advisor, Dr. Sam Legvold, for making this so. His patience, understanding, and guidance have set an example that I will always value highly.

This work would not have been possible without the assistance of the metallurgists at the Ames Laboratory. In particular, Mr. B. J. Beaudry, Dr. K. A. Gschneidner, Jr., Mr. O. D. McMasters, and Mr. J. O. Moorman have been most cooperative in preparing samples and in teaching me the fundamentals of materials science. I also wish to thank Mr. D. W. Jones for allowing me the use of the S.S.E. Nd sample.

The faculty of Iowa State and fellow students have been most friendly and helpful. Many people deserve recognition, but I wish to thank, in particular, Dr. Paul Burgardt and Mr. John Queen. They were always available for helping with equipment or discussing problems. Mr. Dave Oesper and Mr. Darryl Francois helped with the equipment building and computer programming. I also would like to thank Ms. Lynn Rausch for typing and editing this manuscript.

Special thanks go to my wife, Liane, for her support. Her patience and encouragement were a welcomed relief from the problems of graduate study.

IX. APPENDIX

A. Thermoelectric Power of Ce in a Crystal Field

The theory of Bhattacharjee and Coqblin (52) for the thermopower of Ce compounds and alloys starts with a Ce ion (J = 5/2) in a metallic host. The crystal field splits the six-fold degenerate ground state into three doublets (hexagonal field) or a doublet and a quartet (cubic field). Each crystal field level M has an energy E_M. The Anderson hamiltonian is used which becomes, after applying the Schrieffer-Wolff transformation (43),

$$H = \sum_{kM} \varepsilon_k n_{kM} + \sum_M E_M n_M - \sum_{kk'MM'} J_{MM'} C^+_{k'M'} C_{kM} C^+_M C_{M'} + \sum_{kk'M} V_{MM} C^+_{k'M} C_{kM} , \tag{62}$$

where C^+_{kM} is the creation operator for a conduction electron of energy ε_k in the partial-wave state M (in the subspace of ℓ=3, s=1/2, and j=5/2), C^+_M is the creation operator of an electron in the localized state in the crystal field level M, and n_{kM} and n_M are the corresponding number operators. V_{MM} is the direct potential scattering interaction. The $J_{MM'}$ are the 4f--conduction electron exchange coupling parameters given by

$$J_{MM'} = (1/2)\ (|V_{kf}|^2)\ (1/E_M + 1/E_{M'}) \tag{63}$$

where V_{kf} is the matrix element of mixing between the 4f and the conduction electrons. The $J_{MM'}$ have a cut off D such that $J_{MM'} = 0$ if $|\varepsilon_k|$ or $|\varepsilon_{k'}|$ is greater than D. The thermoelectric power is calculated from the formula

$$S = \frac{1}{eT} \frac{\int_{-\infty}^{\infty} \varepsilon_k \, (-\partial f_k/\partial \varepsilon_k) \, \tau_k \, d\varepsilon_k}{\int_{-\infty}^{\infty} (-\partial f_k/\partial \varepsilon_k) \, \tau_k \, d\varepsilon_k} \tag{64}$$

where f_k is the Fermi function

$$f_k = (1 + \exp(\varepsilon_k/k_B T))^{-1} \tag{65}$$

and τ_k is the relaxation time of a conduction electron. This is calculated using the Kondo method (40) of calculating the scattering amplitude in the second Born approximation. This must be calculated to the third order perturbation term in the presence of a crystal field.

The presence of several crystal field eigenstates complicates the evaluation of τ_k. The procedure is to approximate f_k by 1/2 in some of the perturbation theory expressions. The final result is

$$S = (k_B/e)(n(\varepsilon_F)/R) \sum_{i<\ell} (\gamma_i^\ell - \gamma_\ell^i) \, G_1(\Delta_{\ell i},0) \ , \tag{66}$$

where $n(\varepsilon_F)$ is the density of states at the Fermi level, R is an energy independent factor, γ_i^ℓ contains the coupling constants V_{ii} and $J_{i\ell}$, and $\Delta_{\ell i}$ is the crystal field splitting between the ℓ and i levels. $G_1(\Delta,0)$ is a functional defined by

$$G_1(\Delta,0) = \frac{\Delta}{kT} \{1 + \frac{\Delta}{2\pi T} \, \mathrm{Im} \, \psi'(i\frac{\Delta}{2\pi T}) \ , \tag{67}$$

where ψ' is the trigamma function. Other notation used by Reference 52 is that α_i is the degeneracy of the ith crystal field level and v_{MM} is a direct scattering potential defined by

$$v_{MM} = V_{MM} - J_{MM} \langle n_M \rangle \ . \tag{68}$$

For Ce, $\sum_M \langle n_M \rangle = 1$. In practice v_{MM} is assumed to be independent of M.

Bhattacharjee and Coqblin applied this theory to data on $CeAl_3$. They obtained a crystal field energy of 255K from the thermopower data, 113.6K from the resistivity data, and 280K from the magnetic susceptibility data.

To fit the $Ce_{95}La_5$ data in Figure 25, the crystal field levels are held fixed at the measured values. The values of V_{kf} and D are left constant and $n(\varepsilon_F)$ is chosen to be the density of states of pure lanthanum. The values of all the parameters used in the fit in Figure 25 are given in Table 3.

Table 3. Parameters used in the fit to S(T) of $Ce_{95}La_5$

Parameter	Cubic sites	Hexagonal sites
V_{kf}	0.07 eV	0.07 eV
$n(\varepsilon_F)$	2.2 states/eV atom	2.2 states/eV atom
D	850K	850K
α_1	2	2
α_2	4	2
α_3	0	2
Δ_{21}	206K	98K
Δ_{31}		113K
J_{11}	-0.37 eV	-0.1 eV
v	-0.33 eV	-0.4 eV

B. Tabulation of Experimental Data

The temperatures are recorded in degrees K, the electrical resistivity in units of μΩ-cm, and the thermoelectric power in units of μV/K.

Table 4. Electrical resistivity of a-axis Nd

T	ρ	T	ρ	T	ρ
1.35	4.561	5.80	7.571	12.50	11.36
1.70	4.660	6.00	7.744	13.00	11.55
1.80	4.670	6.20	7.936	13.50	11.74
2.00	4.748	6.40	8.107	14.00	11.93
2.20	4.824	6.60	8.292	14.50	12.10
2.40	4.901	6.80	8.444	15.00	12.26
2.70	5.028	7.00	8.655	15.50	12.45
2.80	5.077	7.20	8.830	16.00	12.64
3.00	5.171	7.40	9.002	16.50	12.87
3.20	5.298	7.60	9.160	17.00	13.05
3.40	5.415	7.80	9.308	17.50	13.26
3.60	5.534	8.00	9.439	18.00	13.44
3.80	5.674	8.20	9.553	18.50	13.63
4.00	5.802	8.40	9.650	19.00	13.79
4.20	5.955	8.60	9.753	19.50	13.96
4.30	6.054	8.80	9.854	20.0	14.13
4.40	6.122	9.00	9.942	20.5	14.26
4.60	6.321	9.50	10.179	21.0	14.42
4.80	6.506	10.00	10.381	22.0	14.63
5.00	6.689	10.50	10.596	24.0	15.30
5.20	6.904	11.00	10.782	27.0	16.26
5.40	7.131	11.50	10.977	30.0	17.31
5.60	7.369	12.00	11.14	34.0	18.75

Table 4. Continued

T	ρ	T	ρ	T	ρ
38.0	20.16	86.0	35.57	210.6	59.13
42.0	21.72	98.0	38.12	228.9	61.99
47.5	24.12	110.5	40.90	248.6	64.90
53.0	26.51	122.5	43.70	256.2	65.98
59.0	27.54	139.3	46.73	266.4	67.46
64.0	29.18	153.0	49.50	278.2	69.15
71.6	31.36	171.6	52.54	288.8	70.56
76.5	32.72	191.3	56.08	300.6	72.15
77.7	33.47				

Table 5. Electrical resistivity of c-axis Nd

T	ρ	T	ρ	T	ρ
1.35	2.298	4.20	3.672	6.80	5.735
1.70	2.396	4.30	3.791	7.00	5.916
1.80	2.427	4.40	3.853	7.20	6.060
2.00	2.494	4.60	4.026	7.40	6.195
2.20	2.567	4.80	4.180	7.60	6.295
2.40	2.631	5.00	4.351	7.80	6.401
2.70	2.758	5.20	4.560	8.00	6.499
2.80	2.825	5.40	4.730	8.20	6.579
3.00	2.915	5.60	4.911	8.40	6.652
3.20	3.047	5.80	5.078	8.60	6.721
3.40	3.161	6.00	5.193	8.80	6.814
3.60	3.282	6.20	5.335	9.00	6.899
3.80	3.411	6.40	5.456	9.50	7.065
4.00	3.548	6.60	5.603	10.00	7.230

Table 5. Continued

T	ρ	T	ρ	T	ρ
10.50	7.387	19.00	9.70	77.7	22.30
11.00	7.535	19.50	9.77	86.0	23.72
11.50	7.674	20.0	9.83	98.0	25.56
12.00	7.79	20.5	9.89	110.5	27.52
12.50	7.96	21.0	9.97	122.5	29.49
13.00	8.15	22.0	10.12	139.3	31.77
13.50	8.29	24.0	10.42	153.0	33.72
14.00	8.43	27.0	10.98	171.6	36.11
14.50	8.54	30.0	11.63	191.3	38.96
15.00	8.64	34.0	12.52	210.6	42.05
15.50	8.78	38.0	13.43	228.9	44.45
16.00	8.94	42.0	14.53	248.6	46.94
16.50	9.11	47.5	15.96	256.2	48.11
17.00	9.26	59.0	18.27	266.4	49.56
17.50	9.40	64.0	19.44	278.2	50.89
18.00	9.49	71.6	20.90	288.8	52.19
18.50	9.62	76.5	21.79	300.6	56.47

Table 6. Electrical resistivity of dhcp La, from Legvold *et al.* (62)

T	ρ	T	ρ	T	ρ
5.08	0.00	6.05	0.284	11.98	0.967
5.12	0.056	6.23	0.443	14.02	1.299
5.16	0.250	6.56	0.458	16.16	1.725
5.20	0.266	7.00	0.483	18.02	2.156
5.34	0.270	8.00	0.546	19.98	2.692
5.60	0.273	10.04	0.726	23.0	3.21

Table 6. Continued

T	ρ	T	ρ	T	ρ
26.9	4.48	112.0	30.15	215.9	50.66
31.0	5.92	117.0	31.33	221.9	51.65
35.0	7.35	124.0	32.88	225.5	52.23
39.6	9.02	129.0	33.99	229.5	52.96
44.0	10.49	134.8	35.24	231.3	53.24
48.2	11.94	138.5	36.05	240.7	54.67
52.6	13.43	144.0	37.21	245.5	55.52
56.0	14.56	149.5	38.36	250.7	56.22
58.1	15.30	155.0	39.47	256.0	57.02
66.0	17.69	160.1	40.47	259.8	57.66
71.0	19.15	163.8	41.19	265.2	271.8
76.2	20.88	175.0	43.34	271.8	59.27
77.5	21.12	180.6	44.40	279.3	60.30
80.0	21.85	184.9	45.22	284.8	60.98
85.1	23.30	190.0	46.14	289.3	61.59
89.9	24.68	196.0	47.22	292.3	61.97
96.0	26.21	202.5	48.37	296.4	62.47
101.0	27.45	207.9	49.29	299.9	62.86
107.0	28.89				

Table 7. Thermoelectric power of a-axis Nd

T	S	T	S	T	S
1.93	-0.46	3.39	-0.92	7.28	-1.96
2.05	-0.53	3.64	-0.96	8.10	-2.14
2.50	-0.65	4.22	-1.05	9.08	-2.28
2.75	-0.75	5.59	-1.29	9.67	-2.45
3.12	-0.83	6.47	-1.69	10.13	-2.54

Table 7. Continued

T	S	T	S	T	S
10.71	-2.63	30.6	-4.75	133.1	-5.48
11.38	-2.79	37.2	-4.94	148.1	-5.46
12.24	-3.02	41.7	-5.04	157.3	-5.41
13.23	-3.31	47.1	-5.24	171.1	-5.31
14.43	-3.47	51.8	-5.27	185.3	-5.17
15.83	-3.78	57.6	-5.19	199.3	-4.98
17.75	-3.92	65.0	-5.15	210.3	-4.81
19.14	-4.14	76.1	-5.22	224.9	-4.56
20.46	-4.19	86.6	-5.36	239.4	-4.36
22.3	-4.28	94.3	-5.39	253.1	-4.12
24.1	-4.44	105.1	-5.47	266.1	-3.81
26.1	-4.55	111.5	-5.51	279.0	-3.53
28.0	-4.65	121.0	-5.50	293.1	-3.13

Table 8. Thermoelectric power of c-axis Nd

T	S	T	S	T	S
2.53	0.714	5.30	0.220	8.23	-0.07
2.89	0.724	5.44	0.165	8.38	-0.09
3.17	0.742	5.56	0.143	8.58	-0.13
3.45	0.711	5.66	0.122	9.18	-0.21
3.79	0.688	5.87	0.063	9.33	-0.25
4.06	0.627	6.11	0.023	9.85	-0.34
4.27	0.565	6.40	-0.023	10.17	-0.39
4.47	0.500	6.73	-0.035	10.51	-0.45
4.75	0.431	7.12	-0.012	10.80	-0.52
5.07	0.343	7.53	-0.00	11.41	-0.61
5.17	0.290	8.01	-0.04	12.36	-0.74

Table 8. Continued

T	S	T	S	T	S
13.06	-0.84	24.29	-2.62	81.4	-2.52
13.79	-0.94	25.60	-2.63	86.9	-2.53
14.42	-1.03	28.61	-2.66	95.2	-2.65
15.49	-1.17	30.69	-2.64	104.2	-2.71
16.28	-1.31	33.0	-2.61	113.0	-2.75
17.06	-1.47	33.6	-2.55	125.6	-2.82
17.73	-1.64	35.3	-2.54	134.1	-2.91
18.21	-1.76	37.0	-2.54	148.0	-2.94
18.73	-1.93	39.6	-2.57	171.2	-3.03
19.28	-2.08	43.5	-2.55	191.6	-3.02
19.88	-2.24	46.8	-2.55	218.8	-2.91
20.71	-2.42	51.2	-2.56	227.8	-2.88
21.43	-2.56	56.0	-2.62	248.2	-2.73
22.33	-2.59	60.8	-2.60	269.8	-2.53
23.28	-2.59	70.6	-2.56	291.6	-2.36

Table 9. Thermoelectric power of $Ce_{95}La_5$

T	S	T	S	T	S
2.04	-2.79	3.90	-3.15	5.53	-2.94
2.20	-2.90	4.05	-3.13	5.70	-2.96
2.37	-3.00	4.23	-3.06	5.92	-2.96
2.56	-3.09	4.51	-3.04	6.04	-2.98
2.79	-3.16	4.62	-3.03	6.27	-3.03
2.95	-3.19	4.75	-2.99	6.59	-3.12
3.09	-3.21	4.87	-2.98	6.93	-3.14
3.28	-3.25	5.01	-2.96	7.36	-3.21
3.47	-3.24	5.28	-2.92	7.57	-3.21
3.73	-3.17	5.38	-2.91	8.20	-3.19

Table 9. Continued

T	S	T	S	T	S
8.60	-3.10	13.58	-0.64	79.0	12.02
9.05	-3.02	13.73	-0.57	85.3	11.71
9.75	-2.72	13.87	-0.53	91.2	11.51
9.99	-2.60	14.05	-0.45	96.2	11.13
10.19	-2.58	14.15	-0.41	103.2	10.95
10.34	-2.44	14.32	-0.35	110.0	10.49
10.50	-2.37	14.47	-0.29	116.7	10.04
10.64	-2.28	14.68	-0.23	123.4	9.63
10.78	-2.20	15.18	-0.12	130.0	9.27
10.92	-2.11	16.31	0.12	137.0	8.79
11.05	-2.03	18.29	0.79	143.5	8.43
11.17	-1.96	20.13	1.36	153.0	7.89
11.29	-1.88	22.50	2.11	159.6	7.59
11.44	-1.80	25.02	3.14	168.3	7.15
11.57	-1.73	27.17	3.92	176.6	6.78
11.70	-1.66	29.8	4.91	185.3	6.49
11.82	-1.57	32.8	6.16	193.3	6.22
11.94	-1.52	33.6	6.63	206.3	5.87
12.06	-1.44	36.1	7.37	213.0	5.71
12.19	-1.37	40.9	8.85	220.7	5.53
12.32	-1.31	42.9	9.36	228.6	5.36
12.44	-1.23	45.7	9.92	237.4	5.15
12.59	-1.14	49.4	10.51	246.2	5.01
12.72	-1.09	53.4	10.97	254.6	4.88
12.89	-1.01	56.7	11.35	264.1	4.71
13.06	-0.91	59.0	11.54	272.1	4.63
13.16	-0.85	62.2	11.75	279.7	4.56
13.34	-0.76	64.8	11.82	287.3	4.49
13.41	-0.71	66.4	11.94	296.3	4.36

Table 10. Thermoelectric power of dhcp La

T	S	T	S	T	S
3.80	0.02	20.76	-2.70	104.5	-2.81
4.13	-0.01	22.79	-2.82	110.8	-2.81
4.62	-0.06	25.58	-2.91	117.7	-2.81
4.80	-0.14	28.58	-3.08	125.2	-2.76
4.98	-0.21	31.41	-3.17	133.6	-2.75
5.37	-0.33	34.5	-3.19	143.7	-2.70
5.60	-0.42	38.3	-3.21	153.3	-2.64
5.86	-0.54	42.2	-3.18	163.4	-2.58
6.09	-0.63	45.6	-3.16	172.2	-2.53
6.47	-0.72	48.7	-3.18	183.2	-2.42
7.02	-0.85	52.1	-3.11	193.7	-2.30
7.56	-0.97	56.0	-3.08	203.2	-2.19
8.01	-1.07	61.2	-3.01	213.2	-2.08
8.89	-1.24	64.6	-2.96	224.0	-1.93
9.87	-1.41	67.8	-2.93	236.1	-1.75
11.07	-1.65	71.6	-2.88	248.3	-1.56
12.19	-1.79	75.3	-2.80	260.7	-1.34
13.33	-1.96	78.2	-2.80	274.0	-1.11
14.81	-2.15	84.7	-2.75	286.2	-0.90
16.76	-2.39	89.5	-2.77	296.1	-0.74
18.96	-2.58	97.3	-2.81		

Table 11. Thermoelectric power of fcc La

T	S	T	S	T	S
4.50	-0.01	28.7	-1.87	100.6	-0.57
4.80	-0.02	31.9	-1.83	105.3	-0.53
4.93	-0.04	33.4	-1.77	112.6	-0.44
5.15	-0.09	35.4	-1.71	116.0	-0.40
5.56	-0.15	37.3	-1.64	125.0	-0.33
5.80	-0.24	39.9	-1.63	134.5	-0.25
6.14	-0.48	42.1	-1.62	139.8	-0.21
6.57	-0.71	43.8	-1.62	150.2	-0.11
6.86	-0.76	46.5	-1.61	155.9	-0.05
7.31	-0.85	49.3	-1.58	167.0	0.05
7.96	-0.96	51.9	-1.50	174.8	0.09
9.45	-1.22	54.8	-1.45	182.6	0.24
10.33	-1.37	58.1	-1.39	192.9	0.35
11.24	-1.45	61.3	-1.31	201.7	0.45
12.16	-1.57	64.2	-1.23	212.5	0.59
13.03	-1.67	66.7	-1.15	223.8	0.73
15.11	-1.74	69.0	-1.07	235.8	0.87
16.87	-1.87	72.2	-0.98	247.4	1.01
18.11	-1.89	76.0	-0.89	257.8	1.16
19.94	-1.92	81.7	-0.75	271.3	1.33
22.8	-1.93	87.5	-0.63	283.6	1.47
26.0	-1.89	93.4	-0.63		